1   **Mouse retinal cell behaviour in space and time using light sheet fluorescence**

2   **microscopy**

3

4   Claudia Prahst[*1#], Parham Ashrafzadeh[2#], Kyle Harrington[1,π], Lakshmi Venkatraman[1,2], Mark

5   Richards[2], Ana Martins Russo[3], Kin-Sang Cho[4,5], Karen Chang[4], Thomas Mead[8], Dong Feng

6   Chen[4], Douglas Richardson[6], Lena Claesson-Welsh[2], Claudio Franco[3], Katie Bentley[*1,2,7,8,9]

7   [1] Center for Vascular Biology Research and Department of Pathology, Beth Israel Deaconess

8   Medical Center and Harvard Medical School, Boston, MA 02215, USA.

9   [2] The Beijer Laboratory, Department of Immunology, Genetics and Pathology, Uppsala

10   University, Uppsala, Sweden.

11   [3] Instituto de Medicina Molecular, Lisbon, Portugal

12   [4] Schepens Eye Research Institute of Massachusetts Eye and Ear, Department of

13   Ophthalmology, Harvard Medical School, Boston, MA 02114, USA.

14   [5] Geriatric Research Education and Clinical Center, Office of Research and Development, Edith

15   Nourse Rogers Memorial Veterans Hospital, Bedford, MA 01730, USA.

16   [6] Harvard Center for Biological Imaging, Department of Molecular and Cellular Biology, Harvard

17   University, Cambridge, MA 02138, USA.

18   [7] Biomedical Engineering Department, Boston University, Boston, MA 02215 USA

19   [8] The Francis Crick Institute, 1 Midland Road, London UK

20   [9] Department of Informatics, Faculty of Natural and Mathematical sciences, Kings College

21   London, UK

22   [π]Current address: Virtual Technology and Design, University of Idaho, Moscow, ID 83844, USA.

23   [#] Contributed equally to this work.

24   *Corresponding authors

25   Katie.bentley@kcl.ac.uk / katieab@bu.edu

26   Claudia.prahst@gmail.com

27

28 **Abstract**

29 As the general population ages and the incidence of diabetes increases epidemically, more

30 people are affected by eye diseases, such as retinopathies. It is therefore critical to improve

31 imaging of eye disease mouse models. Here, we demonstrate that 1) rapid, quantitative 3D and

32 4D (time lapse) imaging of cellular and subcellular processes in the murine eye is feasible, with

33 and without tissue clearing, using light-sheet fluorescent microscopy (LSFM) and 2) LSFM

34 readily reveals new features of even well studied eye disease mouse models, such as the

35 Oxygen-Induced Retinopathy (OIR) model. Through correlative LSFM-Confocal imaging we find

36 that flat-mounting retinas for confocal microscopy significantly distorts tissue morphology. The

37 minimized distortion with LSFM dramatically improved analysis of pathological vascular tufts in

38 the OIR model revealing "knotted" morphologies, leading to a proposed new tuft nomenclature.

39 Furthermore, live-imaging of OIR tuft formation revealed abnormal cell motility and altered

40 filopodia dynamics. We conclude that quantitative 3D/4D LSFM imaging and analysis has the

41 potential to advance our understanding of pathological processes in the eye, in particular neuro-

42 vascular degenerative processes.

43

44

45

46

47

48

49

50

51

52

53

Introduction

54

55   Eye diseases, such as diabetic retinopathy, age-related macular degeneration, cataract,

56   and glaucoma are becoming increasingly common with the increased age of the general

57   population. Although advances in understanding and treating eye diseases have been made,

58   the molecular mechanisms involved are still not fully understood. We believe that is partially due

59   to the inadequate ability to image eye tissue in its natural, spherical state, to reveal the many

60   distinct layers with interacting cell types oriented differentially within or between the layers.

61   Optical Coherence Tomography (OCT) is an established medical imaging technique that uses

62   light to capture micrometer-resolution, three-dimensional images non-invasively, now widely

63   used as a diagnostic tool (Srinivasan et al. 2006; Huber et al. 2009). Its main strength lies in

64   revealing information on tissue depth preserving the eyes natural state. However, its limitation

65   lies in not being able to provide a wide field of view, cellular or molecular information.

66   Furthermore, being a non-fluorescent method, specific proteins cannot be labelled and tracked

67   to investigate mechanism.   Currently only confocal microscopy can deliver this detailed

68   fluorescently labelled information (Del Toro et al. 2010), but the 3D nature of the tissue is likely

69   distorted during flat-mounting and it is currently not known to what extent this might impact the

70   obtained results. For instance, the vascular biology field is one clear example where these

71   limitations can have a substantial impact. The mouse retina is a common model used to study

72   vascular development and disease; confocal imaging approaches have been used to measure

73   vessel morphology, vascular malformations, junctional organization, and pathological tuft

74   formation (Gerhardt et al. 2003; Bentley et al. 2014; Stahl et al. 2010). Moreover, vessel

75   diameters are now being used to predict blood flow (Bernabeu et al. 2014, Baeyens et al.,

76   2016). Distortions arising from confocal flat-mounting could therefore have important

77   ramifications for the overall conclusions of several studies.

78   Changes in cellular and tissue morphology are a hallmark of many eye diseases. For

79   instance, retinopathy of prematurity and diabetic retinopathy are characterized by excessive,

80 bulbous and leaky blood vessels that protrude out of their usual layered locations. These

81 malformed vessels cause many problems including the generation of abnormal mechanical

82 traction, which pulls on the different layers, eventually leading to detachment of the retina

83 (Nentwich & Ulbig 2015; Hartnett 2015). Yet, very limited information has arisen on the

84 conformation and morphogenesis mechanisms of these vascular tuft malformations, despite a

85 wealth of confocal studies of the related Oxygen Induced Retinopathy (OIR) mouse model

86 (Connor et al. 2009).

87 Another limitation of confocal microscopy for imaging of mouse retinal angiogenesis is

88 the inability to perform live imaging of endothelial cell dynamics. Endothelial cells move and

89 connect in highly dynamic, complex ways to generate the extensive vascular networks required

90 to perfuse the retina over time (angiogenesis). Whilst live-imaging techniques of blood vessels

91 exist, such as the dorsal skinfold chamber or the cranial window (Brown et al. 2010), it is not

92 possible to translate those to study retinal angiogenesis, as the mouse pups are very small,

93 making it hard to access the retina tissue. There are a small number of reports on *ex vivo* live-

94 imaging of the retinal vasculature with confocal microscopy, but with limited success as

95 flatmounting the retina for live-imaging takes time from dissection to culture, and it is necessary

96 to physically force the tissue onto the membrane, disturbing local tissue arrangement and

97 mechanics (Sawamiphak et al. 2010, Rezzola et al. 2013). Furthermore, photobleaching,

98 phototoxicity and long acquisition times continue to remain an issue.

99 Recent advances in Light Sheet Fluorescence Microscopy (LSFM) have demonstrated

100 its strength for allowing the rapid acquisition of optical sections through thick tissue samples

101 such as mouse brains (Stelzer 2014). Instead of illuminating or scanning the whole sample

102 through the imaging objective, as in wide-field or confocal microscopy, the sample is illuminated

103 from the side with a thin sheet of light. Thus, in principle LSFM would require little interference

104 with the original spherical eye tissue structure, avoiding distortion of the tissue with flat-

105 mounting. Moreover, LSFM is becoming a gold-standard technique to perform live-imaging in

106   whole organs/organisms because it permits imaging of thick tissue sections without disturbing

107   the local environment, while also reducing photobleaching and phototoxicity (Stelzer 2014;

108   Reynaud et al. 2014). Thus, here we investigate the feasibility, advantages and disadvantages

109   of LSFM for imaging the mouse eye for development or disease studies. We present an

110   optimized LSFM protocol to rapidly image neurovascular structures, across scales from the

111   entire eye to subcellular components in mouse retinas. We investigate the pros and cons of

112   LSFM imaging of vessels over standard confocal imaging techniques in early mouse pup

113   retinas. Importantly, we also demonstrate the benefits of LSFM using the OIR mouse model,

114   where we discover previously unappreciated new spatial arrangements of endothelial cells in

115   the onset of vascular tuft malformations due to the improved undistorted, 3D and 4D imaging

116   capabilities of LSFM.

117   We conclude that LSFM quantitative 3D/4D imaging and analysis has the potential to

118   advance our understanding of healthy and pathological processes in the eye, with a particular

119   relevance for the vascular and neurovascular biology fields, as well as Ophthalmology.

120

6

121 **Results**

122 **LSFM enables rapid 3D imaging of mouse eyes, and in particular retinas, in their natural**

123 **state**

124 To visualize the retinal vasculature using epifluorescence or confocal microscopes, the retina is

125 flat-mounted by making four incisions before adding a cover slip containing mounting medium

126 onto glass slides (Fig. 1a, upper panel). To image samples using LSFM, however, samples are

127 suspended in their natural state in low-melting agarose (Fig. 1a, lower panel). This enables

128 imaging of the vasculature of large and intact samples such as the whole eyeball (minus the

129 sclera and cornea) (Fig. 1b), the iris (Fig. 1c), or the optic nerve (Fig. 1d). Using LSFM, it was

130 possible to observe the superficial, intermediate and deep vascular plexus (Fig. 1e and Suppl.

131 Fig. 1b) of a retina in its native conformation (Fig. 1f). In contrast to imaging the retinal

132 vasculature using the confocal microscope, where stacks contain 8 - 15 images, acquiring a

133 stack of the retina using LSFM contains 200 - 300 images, but the imaging time is much shorter

134 (~60 sec vs. ~10 min).

135 Imaging the iris microvasculature (Fig. 1c) surprisingly revealed that the vasculature

136 network is immature at P15 (Fig. 1b, Suppl. Fig. 1), and that it remodels into a mature network

137 in adulthood (Fig. 1c). A network of capillaries was visible at P15, whereas the adult

138 microvasculature consisted of radial branches of small vessels and capillaries in a relatively

139 linear pattern. The major arterial circles (MICs) around the iris root were developed in both P15

140 and adult mice (Fig. 1c and Suppl. Fig. 1a, yellow arrows). The images generated from adult

141 mice using LSFM are consistent with a previous report using OCT to image the iris

142 microvasculature (Choi et al. 2014). Using LSFM, the vessels appeared straighter, and the

143 MICs were not as close to the iris root, which could be because OCT involves live-imaging of

144 the vasculature, without mechanically removing the sclera and cornea.

145 We next tested whether LSFM could resolve subcellular structures in the retinal

146 vasculature such as the Golgi apparatus, which has recently been shown to be important for

7

147 inferring cell polarity during vessel regression (Franco, C.A. et al. 2015). We found it feasible to

148 stain and image the Golgi organelle (Golph4, Alexa 647) and the collagen IV-containing

149 basement membrane around the vessels (Suppl. Fig. 1c, d). On static images of mice

150 expressing lifeAct-enhanced green fluorescent protein (EGFP) we performed deconvolution to

151 reduce the light scattering effects and found this gave a marked improvement to the resolution

152 of actin bundles within endothelial cells (Suppl. Fig. 1e-i). Taken together, LSFM can rapidly

153 generate 3D images of the murine eye in its native form across scales, with tissue, cellular and

154 subcellular resolution.

155

156 **LSFM enables concurrent imaging of retinal cell types within and between the retinal**

157 **layers**

158 A growing number of reports show that neurovascular interactions in the eye are important

159 during development and disease progression (Akula et al. 2007; Narayanan et al., 2014;

160 Nentwich and Ulbig, 2015; Usui et al. 2015; Verheyen et al. 2012). Neurons and vessels are

161 however currently difficult to image in the same retinal tissue across all layers, without distortion

162 due to the way they are arranged in the retina (Fig. 2a, b). Neurons are currently imaged by

163 making vertical sections, orthogonal to the three vascular layers (the superficial, intermediate

164 and deep plexus) (Fig. 2b "side view"), on paraffin or cryo-embedded retinas, which necessarily

165 means losing the ability to observe vascular branching in the horizontal layer in the same tissue.

166 Likewise, studies focused on the retinal vasculature use whole mount images of the retina

167 viewed from above (Fig. 2b, "top view") using horizontal optical sections (Usui et al. 2015),

168 which does not allow proper imaging of retinal neurons spanning between the layers because of

169 insufficient z-resolution in confocal microscopy. Thus, we next investigated whether concurrent

170 imaging of neurons and vessels in the same sample might be achieved with the optical

171 sectioning and rotational viewing capacity of LSFM.

172   We found that eye cups from P3 C57BL/6 Thy1-YFP mice, labelling retinal ganglion cells

173   in yellow combined with IsolectinB4 labeled vasculature provided 3D high resolution images

174   without the need for tissue clearing (Fig. 2c, d, Movie S1). However, we found that including

175   lipid removal/permeabilization as part of a full tissue clearing protocol further improves

176   resolution for eye cups at later stages of development, when more of the retinal layers have

177   formed (Fig. 2e-h), as it decreases the scattered light caused by imaging thicker tissue with the

178   light sheet (Richardson & Lichtman 2015).

179   We tested several different clearing methods to see which was better suited to retinal

180   tissue. We first tested the aqueous-based clearing methods ScaleA2 and FRUIT (Hou et al.

181   2015; Hama et al. 2011). However, these clearing methods did not lead to higher quality images

182   and made tissue-handling very difficult during imaging due to the high viscosity of the FRUIT

183   clearing agent. We also tested the passive aqueous-based methods CUBIC-R (Kubota et al.

184   2017) and PROTOS (Murray et al. 2015), but again found little improvement. Since many

185   studies use animals genetically engineered to express fluorescent markers such as Tomato or

186   GFP, we decided not pursue solvent-based clearing methods such as iDISCO, which do not

187   maintain fluorescent protein emission for more than a few days after the clearing process

188   (Renier et al. 2014). Overall, we found PACT was the most efficient and effective clearing

189   method for retinal tissue, likely because it is relatively thin (Yang et al. 2014; Treweek et al.

190   2015a). PACT cleared adult retinas with Draq5 staining, which stains all nuclei, visualizing the

191   inner nuclear layer (INL) and outer nuclear layer (ONL) (Fig. 2f, Movie S2). The deep vascular

192   plexus, visualized by IsolectinB4 staining could be seen between the ONL and INL, whereas the

193   intermediate vascular plexus bordered the INL as expected. The superficial vascular plexus is

194   located on the inner retinal surface together with nuclei of the retinal ganglion cells (Fig, 2f,

195   Movie S2). Adult retinas were co-immunostained for Tuj1 and Calbindin, markers for retinal

196   ganglion cells and horizontal cells, respectively. This immunostaining made it possible to

197   appreciate the distance between these two cell types in the fully developed retina (Fig. 2g,

198   Movie S3).   3D-rendered images of co-staining for smooth muscle actin and collagenIV

199   moreover showed arteries of the superficial vascular plexus covered with smooth muscle cells

200   (Fig. 2h, Movie S4).

201

202   **Vessel distortion due to confocal flatmounting revealed by correlative LSFM-Confocal**

203   **imaging**

204   As vascular measurements taken from confocal images are used as the standard for

205   inferring the actual sizes of vascular structures in the retina, we next aimed to systematically

206   quantify the 3D distortion of vascular structures incurred by flat-mounting and confocal imaging.

207   In order to make direct, quantitative comparisons of the relatively small vessels in the superficial

208   plexus, we used a correlative LSFM-Confocal approach: we first imaged the retinal tissue with

209   LSFM, which retains the natural tissue curvature, then we melted the gel and flat-mounted the

210   same retina onto a coverslip and imaged it again using confocal microscopy (Fig 3a). We first

211   analyzed the largest vessels near the optic nerve and then smaller capillaries in the sprouting

212   vascular front from P4 wt retinas. Images obtained with our correlative LSFM-confocal approach

213   were then brightness/contrast adjusted and cropped and surface rendered using Imaris to focus

214   on small regions of same vessel segments in the corresponding confocal and LSFM images.

215   Dramatically shallower side views and cross-sections of vessels were evident in the confocal

216   images compared to LSFM (Fig. 3b). We next quantified this shift in aspect ratio by measuring

217   the diameter taken across the vessel in XY (hereafter "Width") and down through the Z-axis

218   (hereafter "Depth") in confocal (Fig. 3c). For LSFM images, given the tissue can be at any

219   orientation in the agarose with respect to the objective, the XYZ coordinate system of the image

220   stack is not indicative of the equivalent width/depth measurement in confocal. Therefore, the

221   orientation of the surrounding vascular plexus at the point of the vessel segment was used as a

222   reference surface "plexus plane" to make the corresponding "width" diameter measurement, as

223   it is equivalent to the XY plane in the corresponding confocal image. Similarly, the "depth"

224   diameter in LSFM was defined as perpendicular to the plexus plane and width measurement

225   (equivalent to the diameter through the z-stack in confocal). Vessels were significantly more

226   elliptical (wider and shallower) under confocal than LSFM indicative of being compressed during

227   flat-mounting (Fig. 3d,e).

228

229   **LSFM enables 4D live-imaging with subcellular resolution, revealing rapid, transient "kiss**

230   **and run" tip cell adhesions at the sprouting front.**

231   *Ex vivo* live-imaging could be a useful tool to study tip cell guidance during the angiogenic

232   sprouting process in the mouse retina, but it has proven to be challenging with conventional

233   microscopy. Existing *ex vivo* confocal methods to live-image retinal vasculature, tissue handling

234   leads to damage of the tissue, as it involves either flat-mounting the retinas onto a membrane

235   and then submerging it in medium (Sawamiphak et al. 2010), or cutting the retina into fragments

236   and embedding them in fibrin gels prior to imaging (Rezzola et al. 2013).

237   We therefore established a protocol for live-imaging of the growing retinal vasculature

238   using LSFM. We first crossed mT/mG mice with Cdh5(PAC)-CreERT2 mice and injected them

239   with tamoxifen to induce endothelial GFP expression (Muzumdar et al. 2007; 2010; Wang et al.

240   2010). Surprisingly, connections between ECs formed very rapidly (within 20 min) and

241   regressed just as rapidly (Fig. 4a, Movie S5). Such transient "kiss and run" adhesion and

242   release style interactions between ECs (as opposed to full adhesions or anastomoses, where

243   the connections stably remain) have only been previously reported in glycolysis-deficient ECs *in*

244   *vitro* with "normal" connections being more stable *in vitro* (Schoors et al. 2014). The dynamics *in*

245   *vivo* were therefore assumed to be slower and more stable than *in vitro* live-imaging, however

246   our new observations indicate a very different set of dynamics and inter-cellular behaviors may

247   be at work in the complex *in vivo* tissue. Timing is crucial, as the VEGF gradient dissipates after

248   the retinas are dissected and submerged in agarose, at room air and the tissue is therefore no

249   longer hypoxic. However, the directed growth of the filopodia towards the vascular front in our

250   LSFM movies suggests that this gradient remains intact for at least the first few hours after

251   dissection. We found filopodia length and extension, retraction dynamics quantification feasible

252   (Fig. 7d,e,f). Further back from the sprouting front, in the vascular plexus (Fig. 4b, Movie S6),

253   we occasionally observed the formation of connections over the course of a few hours,

254   however, branch formation was a rare occurrence. Notably, we did not observe EC apoptosis

255   under these imaging conditions indicating conditions are viable.

256   We next assessed the feasibility of using LSFM to live-image intracellular processes.

257   We dynamically imaged mice expressing lifeAct-EGFP, which fluorescently labels F-actin

258   (Fraccaroli et al. 2012) with LSFM and quantified the movements of actin-enriched bundles

259   within the endothelial cell bodies in the sprouting front during developmental angiogenesis.

260   Quantitative subcellular actin live-imaging was found feasible (n=6 retinas) with the average

261   distance travelled by each bundle found to be 2.56 µm (Fig. 4c, movies S7, S8 and S9).

262   Taken together, our LSFM permits the visualization in real-time of cellular movements

263   with subcellular resolution in the mouse retina, with minimal distortion.

264

265   **Three subclasses of pathological retinal neovascular tufts revealed with LSFM**

266   We next sought to image vessels that have grown pathologically, in order to determine whether

267   this imaging method could be used to gain greater insights into eye disease. To this end, we

268   used the OIR model, where mouse pups are placed in 75% oxygen from P7 to P12, and are

269   then kept at room air from P12 to P17 (Connor et al. 2009). During the hyperoxia phase, the

270   vasculature regresses, and in the subsequent normoxia phase, new vessels grow in an

271   abnormally enlarged and tortuous manner (Connor et al. 2009). Furthermore, vessels also start

272   to grow into the vitreal space forming bulbous vessels, known as "vascular tufts", above the

273   superficial vascular layer (Fig. 5a). In the past, it has been difficult to analyze and characterize

274   the growth of these tufts because they are large formations which appear to be distorted by the

275   flat-mounting process. By performing IsolectinB4 and ERG immunostaining to visualize

276   endothelial cells (ECs) and their nuclei, we obtained 3D-reconstructions of the tufts and were

277   able to first classify them into different groups by quantifying both volume and number of nuclei

278   (Fig. 5a,e). As expected, we found that the number of nuclei increased with the size of the tuft

279   (R^2 = 0.83). Interestingly, however we found many small tufts, and only very few large tufts. The

280   smallest tuft we could identify had two nuclei parallel to each other, the cells growing straight up

281   into the vitreous (Fig. 5a, upper panel, Movie S10). We found that most tufts have between 4

282   and 20 nuclei ("Medium tufts", Fig. 5a, second panel row, Movie S11). We also identified a few

283   very "large tufts" with over 20 nuclei (Fig. 5a, third panel row, Movie S12). Next, we quantified

284   the number of connections between the vasculature and the tuft (Fig. 5b). The large tufts had a

285   higher number of connections to the existing vasculature (R^2 = 0.61), however surprisingly for

286   medium and large tufts, despite very different nuclei counts, the tuft volume and number of

287   connections to the plexus remain approximately constant (Fig. 5c). However, the number of

288   connections and tuft volume transition sharply to ~2.5 fold and ~3 fold respectively, when the

289   number of nuclei in the tuft exceeds twenty. This indicates that proliferation or an influx of cells

290   to the tuft does not increase tuft volume, but rather tuft volume only significantly increases when

291   the number of connections to the plexus also increases. Based on this observation, we propose

292   that large tufts are in fact formed by fusion of 2 or 3 medium tufts.

293   We observed that some of the vascular tufts contained highly curved nuclei (Fig. 5a,

294   fourth panel row, yellow arrow, Movie S13). Quantification of the number of curved nuclei/total

295   nuclei in a tuft showed that in small and medium tufts, the number of curved nuclei correlated

296   well with the number of total nuclei (Fig. 5d). In large tufts (over 20 total nuclei), the number of

297   curved nuclei was stable suggesting actually a decline in curved nuclei as the number of cells in

298   the tuft increased. Thus, the relative number of curved nuclei per tuft could also be used as a

299   clear marker to distinguish medium and large tufts. As curved nuclei indicate cells are under

300   severe mechanical strain, twisting or turning them around (Yuntao et al. 2018), this suggests

301   that larger tufts may be more stable and mature, whereas the small and medium ones are under

13

302   more tension, still forming with significant forces curving and pulling the cells around in the tuft.

303   Interestingly, highly curved nuclei have been shown to result in rupture of the nucleus and DNA

304   damage (Yuntao et al. 2018), which may further exacerbate dysfunctional cell behavior in tuft

305   formation. It should be noted that care should be taken to rotate the image stack to confirm

306   nuclear curvature, as two nuclei parallel to each other can look like only one nucleus (Fig. 5a,

307   fourth panel row, blue arrow), emphasizing the importance of 3D imaging with LSFM as rotating

308   and viewing tufts from the side without distortion is not possible with confocal.

309   Finally, to quantify the level of distortion of vascular tufts incurred by flat-mounting and

310   confocal imaging, we compared tuft depth measurements between retinas imaged with confocal

311   and LSFM (depth defined the tuft length orientated perpendicular to plexus plane). The change

312   in depth was particularly striking and more pronounced for larger tuft structures (Fig 5a bottom

313   panels, e), further confirming that LSFM is superior to confocal to image larger structures in the

314   eye.

315

316   **LSFM OIR Case-study: Pathological retinal neovascular tufts have a knotted morphology**

317   In order to gain better resolution to characterize the specific morphology of the different sized

318   tufts we next performed computational image deconvolution on cropped LSFM images of

319   vascular tufts (see Materials and Methods), which helped to decrease the scattered light caused

320   by imaging thicker tissue with the light sheet without the need to clear the tissue (Richardson &

321   Lichtman 2015). Upon deconvolution a dramatic and previously unappreciated "knotted"

322   morphology of the tufts was evident across all tuft classes; often tufts had one or more holes

323   going through (Fig. 6a,b white arrows. Also see Suppl. Fig. 2a,b for more rotational views and

324   original rotational movies S14,S15). To describe these 3D tuft structures in detail, we next

325   explored three systematic approaches: 1) by slowly shifting clipping planes through the tuft from

326   the vitreous facing side to the plexus-connecting side of the tuft it was possible to better

327   appreciate the upper and lower 3D organization of the tuft; 2) carefully rotating and hand-

14

328   drawing the tufts surface rendered structures from every angle and 3) comparing the colour-

329   labeled positions of nuclei to indicate their depth position in the tuft. The first approach revealed

330   that the tuft shown in Fig. 5a fourth panel row, had a figure of eight knot, with two clear holes

331   through the tuft and an unexpected vessel connecting the upper vitreous surface of the tuft to

332   the plexus (Fig. 6c and Suppl. Fig. 2b, blue stars, Movie S13). A combination of the second two

333   approaches revealed a swirl structure to two tufts (small and medium in size) akin to a snake

334   coiling upon itself, with several highly curved nuclei (Fig. 6d-I, Movies S16, S17) and a central

335   hole through the entire tuft. The smaller swirled tuft had two layers, while the medium tuft had

336   three. In both cases the top, vitreous facing surface of the tuft appeared sprout-like with

337   protrusive shapes, a morphology consistent across many tufts, e.g. Suppl. Fig. 2c white arrow

338   and Fig. 7a. Overall, all three approaches were extremely useful for better interpreting these

339   complex 3D structures, providing a much deeper understanding of them than viewing as

340   maximum 2D projections or simply rotated on a screen.

341

342   **4D LSFM live-imaging of the OIR mouse model reveals altered cell dynamics**

343   To gain insights into endothelial cell behavior in vascular tufts, we next imaged the OIR-induced

344   tufts dynamically with LSFM. Thereby, we observed that filopodia extended/retracted from

345   abnormal vascular tufts, similar to what is seen in the extending vascular front during

346   development of the retina vasculature. However, filopodia formed from vascular tufts remained

347   very short (mean 4.3 μm) as compared to normoxia (mean 14.84 μm) (Fig. 7a, d). In OIR,

348   filopodia more rapidly extended and retracted, without making connections (Fig. 7a, e, f, Movie

349   S18). As the VEGF gradient is expected to be disrupted in the OIR model, timing from

350   dissection to imaging is not as crucial. However, most filopodia movements occurred in the first

351   few hours under this pathological condition. When imaging other parts of the OIR retinas to the

352   tufts, we observed intriguing, abnormal EC behaviour. Their movements were undirected and

353   appeared to involve blebbing-based motility (Fig. 7b, c, Movie S20). We observed both cells that

354   were dividing, and undergoing apoptosis (Fig. 7b, Movie S19), which was not observed during

355   normal conditions. This first live imaging of altered cell behavior in the OIR mouse model further

356   highlights the potential of LSFM for new insights into disease processes.

357

358   **Conclusions and Discussion**

359   Although LSFM is becoming increasingly popular, studies to date have not attempted to

360   use it to image eye tissue. We have therefore established the first protocols to image and clear

361   mouse eye tissue using LSFM. Because this protocol utilizes optical sectioning of whole mount

362   tissue, we found that LSFM is a very useful tool to rapidly image and reveal eye tissue at

363   cellular and subcellular resolution without distortion of the sample due to flat-mounting, with the

364   benefit to view and rotate structures in full 3D. As such, the present study provides a highly

365   relevant and improved approach to examine the inter-relationships of normal neurovascular

366   structures and the complex morphology of aberrant vascular structures in disease models,

367   revealing for the first time a knotted morphology to the vascular tufts in OIR. We have also

368   established a clearing protocol for eye tissue. We have furthermore established an *ex vivo* 4D

369   live-imaging method to follow angiogenic growth in the mouse retina in real-time, both during

370   development and under pathological conditions, and quantified that these dynamics are

371   significantly altered in pathological conditions. The acquisition of 3D images of vascular

372   structures at high spatial and temporal resolution within intact ocular tissue is both novel and

373   significant. Overall, we strongly suggest the use of LSFM for 1) the study of larger or more

374   complex 3D tissue structures reaching across the typical retinal layers, which are liable to

375   distortion with standard approaches and 2) dynamic cell and subcellular processes in the mouse

376   eye. We see far-reaching potential of the approach for deeper insights into eye disease mouse

377   models in particular. For example, it would now be feasible to skeletonize larger portions of the

378   vascular network (ultimately, the entire retina vasculature) in order to perform flow simulations

379 and understand how the biomechanical feedback of flow impacts vessel growth in healthy and

380 diseased eyes.

381

382 **LSFM vs Confocal: A Balanced Discussion**

383 ***Benefits of LSFM:*** In general image acquisition with LSFM is widely known to be far faster than

384 confocal due to the illumination of the entire optical plane at once combined with the use of a

385 camera instead of detectors, as noted earlier, an extensive stack of the entire mouse retina can

386 be acquired very quickly using LSFM (~60 sec). 1) LSFM is better for imaging thicker or very

387 large tissues (such as the eye cup, which is thin, but topologically spherical), due to the fast

388 acquisition rates and the large, rotatable sample holder, removing the limited single view point

389 from above with upright microscopes and slide mounting, 2) the illuminated plane generates

390 less photobleaching and faster time frame rates for high temporal resolution live imaging of 3D /

391 very thick tissues. We find LSFM imaging of the retina to be particularly informative over

392 standard confocal microscopy when studying the following specific complex 3D and/or dynamic

393 structures in the eye: 1) the adult retina in full - it is possible to visualize all three vascular layers

394 in the LSFM, including direct cross-sectional viewing of the diving vessels oriented between

395 layers by rotating the sample relative to the objective, which is not possible with confocal.

396 Similarly, the iris and optic nerve can be observed in full, from any angle, undistorted with

397 LSFM. 2) abnormal enlarged vessels/tufts - a newly characterized knotted morphological

398 structure of tufts was revealed due to the improved 3D imaging and rotational viewing possible

399 with LSFM. With confocal imaging the tuft shape can only be inferred from above and we found

400 the depths were significantly distorted and compressed, which is likely why knots have not been

401 described before. Interestingly the VE-cadherin staining of endothelial junctions of several OIR

402 tufts shown in (Bentley et al 2014) indicated there were "holes" through tufts, as no junctional

403 stains were found in clear pillars through them. However, the holes were not easy to confirm by

404 isolectinB4 staining in the same samples, likely due to spreading of the vascular structure when

17

405 it was distorted during flat-mounting. We can confirm here with LSFM there are holes through

406 tufts and that tufts appear to consist of one or more long vessel structures intertwined, swirled

407 and potentially looped upon themselves. 3) Neurovascular interactions in one sample, as

408 neurons and vessels are oriented perpendicular to each other through the retina, they are

409 normally imaged with separate physical sectioning or flattening techniques in either direction,

410 prohibiting their concurrent observation. Optical sectioning of thick tissue and then rotating the

411 undistorted image stacks allows both to be imaged for the first time together. Indeed, obtaining

412 such images from one sample with LSFM will permit the quantification of vessels protruding

413 through the neuronal layers, which is now only possible by performing time-consuming serial

414 block-face scanning electron microscopy (Denk & Horstmann 2004). 4) Live-imaging of

415 developing mouse retinas – this has proven very difficult with *in vitro* methods providing more

416 reliable assays, e.g. embryoid bodies (Kearney & Bautch 2003; Jakobsson et al. 2010).

417 Although embryoid bodies contain some other cell types such as pericytes, they still do not fully

418 reflect the complex and tissue specific *in vivo* retinal environment. Importantly, the vessel-like

419 structure formed in the embryoid bodies have never experienced flow. Moreover, the embryoid

420 bodies are treated with VEGF supplied to the culture medium, while in vivo, endothelial cells are

421 exposed to a VEGF gradient from the astrocyte network below. Our images suggest that the

422 VEGF gradient remains intact in the retina samples for several hours in LSFM imaging.

423 Furthermore, our protocol enables us to follow and quantify filopodia movements from minute to

424 minute, revealing movements never seen before. Thus, we observed astonishing abnormal

425 cellular and subcellular level dynamics under pathological OIR conditions by 4D live LSFM

426 imaging.

427 **Benefits of confocal over LSFM:** Confocal microscopy has a fundamentally higher spatial

428 resolution with less light scatter than LSFM; clearer, more precise images of smaller structures

429 can be obtained, such as endothelial junctions and tip cell filopodia morphology provided the

18

430   tissue sample is amenable to flat mounting without distortion or loss of information – i.e. it is

431   naturally thin cross-sectionally and structures of interest have their main features in the XY

432   plane, not in Z, XZ or YZ. Thus, confocal static imaging of normal developing vessels in a single

433   layer of the retina will still yield better resolution images than LSFM and is very reliable for XY

434   based quantifications such as branch point analysis. However, we find it is not reliable for

435   acquiring accurate quantifications involving depth through Z such as vessel diameters or the

436   morphology of cells that span between the layers (e.g. in the XZ or YZ planes). Thus, overall

437   LSFM is not suggested to replace confocal for static developmental angiogenesis studies.

438   However, to study and measure precise morphological attributes or dynamics of vessels with

439   inherently 3D nature such as vessel radii, enlargements, malformations, diving vessels, iris,

440   optic nerve or the deeper layers we find strong evidence to favour LSFM over confocal imaging.

441   In general, the quantification time was comparable between LSFM and confocal images but

442   there is potential for image analysis to require more effort for LSFM as files can become quickly

443   large due to the rapid imaging (~200GB for static imaging and up to 4TB for live multichannel

444   imaging). If an older eye is being imaged the three vascular layers will be somewhat visually

445   overlapping (e.g. in Supp. Fig. 1b), which could be hard to manually untangle due to the

446   curvature, and as such represents a limitation. The preservation of the tissue depth information

447   in the large z stack however, means by computationally fitting to the local curvature of the eye

448   tissue one could computationally colour code and subtract the retinal layers out for independent

449   viewing and analysis, but this requires more investment than depth colour coding of flat-

450   mounted confocal images (Milde et al. 2013).

451

452   **Vascular Tuft Formation**

453   The OIR model is a commonly used to study retinopathies. The three-dimensional nature of

454   vascular tufts makes them ideal for LFSM and though this is a widely studied mouse model, the

455   improved three-dimensional imaging allowed us to identify several new features of the important

19

456   pathological vessels it generates. Our observations of small, medium and large tuft classes with

457   distinct properties and the observation of more complex knotted, swirling and looping

458   morphologies than previously reported, suggest a new mechanistic explanation is required to

459   understand how and why vessels twist and turn on themselves and why it appears that medium

460   tufts reach a critical size then stop twisting and instead coalesce into larger more stable

461   structures, akin to the development of blood islands in retinal development (Goldie et al., 2008).

462   Nuclei with unusual shapes have previously been identified in abnormally growing

463   tissues, such as cancer (Hida et al. 2004; Kondoh et al. 2013; Versaevel et al. 2012), and to

464   reflect mitotic instability (Gisselsson et al. 2001). It is remarkable that we observed the

465   dramatically curved shape of EC nuclei in tufts. Although it remains unclear whether their

466   unusual shape has consequences for EC function in the tuft, it is tempting to speculate that it

467   would have some bearing on, or is at least be an indicator of abnormal cell behavior. Overall,

468   the ability to rotate the tufts in 3D and view from the side, not just the top, gave a much clearer

469   view of their structure potentiating a detailed analysis of their complex knotted structure in the

470   future. LSFM therefore could greatly improve our understanding of these abnormal vascular

471   formations, already opening up avenues for future studies.

472   Taken together, we propose that tuft formation proceeds as follows 1) small tufts are

473   sprouts from the existing vasculature oriented upwards to the vitreous (e.g. as shown in Fig, 5a

474   top panel) initiating the formation of a new tuft. However, further dynamic study is required to

475   establish whether they are medium tufts that instead are regressing; 2) medium tufts originate

476   from small tufts that continue to sprout, loop and potentially fuse with other upward sprouts (to

477   generate the observed increase in connections to the plexus below), actively swirling and

478   knotting around themselves. Further studies are needed to identify if other cell type/extracellular

479   tissue acts as a scaffold to create the space/holes within them; 3) large tufts form when medium

480   tufts merge with each other whereupon the knotting/swirling process declines (indicated by the

481   plateau in curved nuclei in the large tufts and the sudden jump in tuft volume and connections to

482   the plexus) possibly indicated final stabilization or even a switch to the natural normalization of

483   tufts in this model.

484

Reproducible Live imaging of angiogenesis in the retina

486   Current retinal studies must infer dynamics from static images by hypothesizing what might

487   have happened in real-time to generate the retina's phenotype. For example, CollagenIV-

488   positive and IsolectinB4-negative vessels are considered to be empty membrane sleeves where

489   the vasculature has regressed. It is therefore important to establish reproducible live-imaging

490   methods. It will be interesting to investigate in future live-imaging studies how pervasive the kiss

491   and run behaviors are across the plexus and under different conditions, in order to fully

492   elucidate their functional role. We furthermore demonstrated the potential to quantify diverse

493   subcellular level movements in the cells as proof of concept. The LSFM live imaging protocol is

494   sturdy as indicated from the testing in three different laboratories in three different countries

495   (US, Sweden and Portugal) with different scientists performing the dissections and imaging, on

496   different instruments. As such we can confirm that though challenging, the live imaging protocol

497   has been optimized and is reproducible in different hands.

498

Materials and Methods

Mice

501   mT/mG mice were crossed with cdh5 (PAC) CreERT2 mice (Wang et al. 2010). For live-imaging

502   of retinal angiogenesis during development, mice were injected with 50 µg tamoxifen at

503   postnatal day (P) 1, P2 and P3, and imaged at P4 (Wang et al. 2010). For live-imaging of

504   oxygen-induced retinopathy (OIR) experiments, mice were injected with 100 µg tamoxifen at

505   P13, P14 and P15. The retinal vasculature was imaged at P17. Recombination was confirmed

506   by GFP expression in ECs. Mice used in experiments at Beth Israel Deaconess Medical Center

507   were held in accordance with Beth Israel Deaconess Medical Center IACUC guidelines. Animal

508   work performed at Uppsala University was approved by the Uppsala University board of animal

509   experimentation. Transgenic mice were maintained at the Instituto de Medicina Molecular (iMM)

510   under standard husbandry conditions and under national regulations.

511

512   **Antibodies**

513   IsolectinB4 directly conjugated to Alexa488 and all corresponding secondary alexa conjugated

514   antibodies were obtained from Invitrogen. Isolectin IB4 conjugated with an Alexa Fluor 568 dye

515   was purchased from Thermo Fisher Scientific, MA. Anti-calretinin (ab702) and anti-ERG

516   (ab2513) antibodies were obtained from Abcam. The antibody directed against Calbindin

517   (AB1778) was acquired from Millipore. Anti-Glial Fibrillary Acidic Protein (GFAP) antibody was

518   purchased from Dako (Z0334), anti-CollagenIV from AbD Serotec (2150-1470), biotinylated anti-

519   neuron-specific b-III Tubulin from R&D Systems (Clone TuJ-1, BAM1195), and Cy3-conjugated

520   anti-smooth muscle actin (SMA) antibody was obtained from Sigma Life Science (C6198).

521   Draq5 was obtained from ThermoScientific. Anti-GOLPH4 (ab28049) from Abcam.

522

523   **Immunohistochemistry**

524   Retinas were dissected as previously described (Del Toro et al. 2010). In brief, eyeballs were

525   fixed for 18 min in 4% paraformaldehyde at room temperature. After dissection, retinas were

526   blocked for 1 hour in blocking buffer (TNBT) or Claudio's Blocking Buffer (CBB) for retinas with

527   Golgi stained. CBB consists of 1% FBS (ThermoFisher Scientific), 3% BSA (Nzytech), 0.5%

528   Triton X100 (Sigma), 0.01% Sodium deoxycholate (Sigma), 0,02% Sodium Azide (Sigma) in

529   PBS pH = 7.4 for 2 hr in a rocking platform) for retinas stained for golgi. Thereafter, retinas were

530   incubated overnight in primary antibody in blocking buffer. After extensive washing, retinas were

531   incubated in the corresponding secondary antibody for 2 hours at room temperature. For

532   confocal microscopy, retinas were mounted on glass slides, and for LSFM, retinas were

533   mounted in 2% low-melting agarose. Agarose was melted at >65°C, and then maintained at

22

534   42°C before adding the tissue. To minimize curling of the retina, apply 1-2 drops of low melting

535   agarose on retina and start uncurling the retina before the gel is solidified. It can then be

536   transferred to the cylinder for imaging.

537

538   **PACT clearing of retinas**

539   PACT clearing was performed as previously described (Treweek et al. 2015b). Retinas were

540   dissected and fixed with 4% PFA at 4°C overnight. Samples were incubated overnight at 4°C in

541   ice cold A4P0 (40% acrylamide, Photoinitiator in PBS). The following day, samples were

542   degassed on ice by applying a vacuum to the tube for 30 min, followed by purging with N_2 for 30

543   min. Thereafter, samples were incubated at 37°C for 3h to allow hydrogel polymerization.

544   Excess gel was then removed from the samples, the samples washed in PBS, and incubated at

545   37°C for 6h in 8% SDS/PBS, pH 7.5. Samples were then washed in PBST for 1-2 days,

546   changing wash buffer 4-5 times to remove all of the SDS. Immunostaining was then performed

547   following the same protocol without PACT clearing. Thereafter, the tissue was cleared by at

548   least 48h incubation in RIMS (40 g histodenz in 30 ml of sterile-filtered 0.02 M phosphate buffer,

549   0.01% sodium azide). Cleared retinas were mounted in 5% low-melting agarose/RIMS for LSFM

550   imaging.

551

552   **Live-imaging**

553   For live-imaging, mice were imaged at P4 or P5. The sample chamber was filled with DMEM

554   without phenol red containing 50% FBS and P/S and heated to 37°C. Retinas were quickly

555   dissected in prewarmed HBSS containing penicillin and streptomycin. After dissection, retinas

556   were rapidly cut into quarters (mainly to minimize the datafile size created, the curved form was

557   preserved) and immediately mounted in 1% low melting agarose in DMEM without phenol red

558   containing 50% Fetal Bovine Serum (FBS) and 1x penicillin and streptomycin (P/S). To

23

559 minimize curling of the retina, as with static imaging, apply 1-2 drops of low melting agarose on

560 retina and start uncurling the retina before the gel is solidified. It can then be transferred to the

561 cylinder for imaging.

562

563 **Equipment**

564 All LSFM images were acquired with a Zeiss Z.1 light sheet microscope. The Zeiss objectives

565 used for uncleared tissue and live imaging were Zeiss, RI=1.33, 5x/0.16, and 20x/1.0. For PACT

566 cleared tissue, RI=1.45, 20x/1.0 (5.5mm working distance) was used. All raw data were handled

567 on a high-end DELL workstation (Dual 8-core Xeon Processors, 196GB RAM, NVIDIA Titan

568 Black GPU, Windows 7 64 bit) running ZEISS ZEN (Light sheet edition). Confocal images were

569 taken with the LSM 880 Confocal Microscope.

570

571 **Image Analysis**

572 **Visualization of images in 3D**

573 3D reconstructions of images up to 4 GB were obtained using Imaris software. Fiji was used for

574 reconstruction of images larger than 4 GB. To quantify tuft volumes, Arivis Vision4D software

575 was used.

576

577 **Visualization of live-imaging**

578 To visualize live-images, the maximum intensity projection of each timepoint was made in ZEN

579 (Zeiss). The movies were corrected for drift correction in Fiji using the StackReg plugin and the

580 background subtracted in Fiji using rolling ball background subtraction.

581

582 **Deconvolution**

24

583　In LSFM, when using a high NA (>~0.6) objective, the optical section is determined by the depth

584　of field of the objective and not the light sheet. However, in our system the light sheet is thicker

585　than the objective's depth of field and substantial out-of-focus light is captured relative to

586　confocal. Additionally, thick tissue samples have an intrinsic milky appearance. This lack of

587　clarity undermines sharp images and becomes progressively more of an impediment the deeper

588　one tries to look into a tissue volume. This translucency is caused by heterogeneous light

589　scattering (Richardson & Lichtman 2015). As the tissue used for imaging in LSFM is thick,

590　fluorescent light originating from deep within the tissue is scattered during its travel through the

591　tissue volume, back to the objective. This results in both in- and out-of-focus light arriving at an

592　incorrect position on the camera causing objects to blur.

593　To deconvolve and reduce this light scatter computationally images were split into channels with

594　their respective emission wavelength. Microscopic parameters (including pixel size, objective

595　and excitation wavelength) were inserted into the settings of Huygens software for each channel

596　followed by choosing the signal to noise ratio (SNR) for each image and run the deconvolution

597　with the same settings. The resulted deconvolved images were inserted into Imaris for further

598　analysis in 3D if needed. Huygens software was used for deconvolving all images.

599　**Actin-rich bundles and filopodia tracking.** Tracking was performed manually using

600　ImageJ/Fiji. For filopodia tracking, each filopodia was tracked between each frame of imaging

601　and different analysis was performed. For tracking the actin-rich bundles, the Manual Tracking

602　plugin in Fiji was used to manually select the ROI (=region of interest) and follow the pathway of

603　each trajectory. The trajectories and the pathway were overlaid. Each trajectory could be

604　visualized using Montage function.

605

606　**Acknowledgements**

25

623   **Competing Interests**

624   The authors declare no competing interests.
625
626
627
628   **References**

629   Abe, J. et al., 2016. Light sheet fluorescence microscopy for in situ cell interaction analysis in
630   mouse lymph nodes. *Journal of Immunological Methods*, pp.1–10. Available at:
631   http://linkinghub.elsevier.com/retrieve/pii/S0022175916300151.

632   Akula, J.D. et al., 2007. Rod Photoreceptor Function Predicts Blood Vessel Abnormality in
633   Retinopathy of Prematurity. *Investigative Opthalmology & Visual Science*, 48(9), p.4351.
634   Available at: http://iovs.arvojournals.org/article.aspx?doi=10.1167/iovs.07-0204.

635   Baeyens, N. et al., 2016. Endothelial fluid shear stress sensing in vascular health and disease.
636   *Journal of Clinical Investigation*, 126(3), pp.821–828. Available at:
637   https://www.jci.org/articles/view/83083.

26

Bentley, K., Franco, C.A., Philippides, A., Blanco, R., Dierkes, M., Gebala, V., Stanchi, F., Jones, M., Aspalter, I.M., et al., 2014. The role of differential VE-cadherin dynamics in cell rearrangement during angiogenesis. *Nature Cell Biology*, 16(4), pp.309–321. Available at: http://www.nature.com/doifinder/10.1038/ncb2926.

Bernabeu, M., Jones, M.L., Nielsen, J.H., Krüger, T., Nash, R.W., Groen, D., Schmieschek, S., Hetherington, J., Gerhardt, H., Franco, C. A., Coveney, P. Computer simulations reveal complex distribution of haemodynamic forces in a mouse retina model of angiogenesis11J. R. Soc. Interface http://doi.org/10.1098/rsif.2014.0543

Borgefors, G., 1984. Distance transformations in arbitrary dimensions. *Computer Vision, Graphics, and Image Processing*, 27, pp.321–345. Available at: http://www.sciencedirect.com/science/article/pii/0734189X84900355.

Brown, E. et al., 2010. In vivo imaging of tumors. *Cold Spring Harbor Protocols*, 5(7), pp.1–5.

Connor, K.M. et al., 2009. Quantification of oxygen-induced retinopathy in the mouse: a model of vessel loss, vessel regrowth and pathological angiogenesis. *Nature protocols*, 4(11), pp.1565–1573.

Danielsson, P.-E., 1980. Euclidean distance mapping. *Computer Graphics and Image Processing*, 14(3), pp.227–248. Available at: http://linkinghub.elsevier.com/retrieve/pii/0146664X80900544.

Denk, W. & Horstmann, H., 2004. Serial Block-Face Scanning Electron Microscopy to Reconstruct Three-Dimensional Tissue Nanostructure Kristen M. Harris, ed. *PLoS Biology*, 2(11), p.e329. Available at: http://dx.plos.org/10.1371/journal.pbio.0020329.

Ellenbroek, S.I.J. & van Rheenen, J., 2014. Imaging hallmarks of cancer in living mice. *Nature Reviews Cancer*, 14(6), pp.406–418. Available at: http://www.nature.com/doifinder/10.1038/nrc3742.

Fei, P. et al., 2016. Cardiac Light-Sheet Fluorescent Microscopy for Multi-Scale and Rapid Imaging of Architecture and Function. *Nature Publishing Group*, (October 2015), pp.1–12. Available at: http://dx.doi.org/10.1038/srep22489.

Franco, C.A., Jones,M.L., Bernabeu,M.O., Geudens, I., Mathivet, T., Rosa, A., Lopes, F.M., Lima, A.P., Ragab, A., Collins, R.T., Phng, L-K., Coveney, P., Gerhardt, H., 2015. Dynamic endothelial cell rearrangements drive developmental vessel regression. PLoS biology 13 (4), e1002125

Gerhardt, H. et al., 2003. VEGF guides angiogenic sprouting utilizing endothelial tip cell filopodia. *Journal of Cell Biology*, 161, pp.1163–1177.

Gisselsson, D. et al., 2001. Abnormal Nuclear Shape in Solid Tumors Reflects Mitotic Instability. *The American Journal of Pathology*, 158(1), pp.199–206.

Goldie, L.C., Nix, M.K. & Hirschi, K.K., 2008. Embryonic vasculogenesis and hematopoietic specification. *Organogenesis*, 4(4), pp.257–63. Available at: http://www.ncbi.nlm.nih.gov/pubmed/19337406.

Güç, E. et al., 2014. Long-term Intravital Immunofluorescence Imaging of Tissue Matrix Components with Epifluorescence and Two-photon Microscopy. *Journal of Visualized Experiments*, (86), pp.e51388–e51388. Available at: http://www.jove.com/video/51388/long-term-intravital-immunofluorescence-imaging-tissue-matrix.

Hägerling, R. et al., 2013. A novel multistep mechanism for initial lymphangiogenesis in mouse

682   embryos based on ultramicroscopy. *The EMBO journal*, 32(January), pp.629–44. Available
683   at:
684   http://www.pubmedcentral.nih.gov/articlerender.fcgi?artid=3590982&tool=pmcentrez&rend
685   ertype=abstract.

686 Hama, H. et al., 2011. Scale: a chemical approach for fluorescence imaging and reconstruction
687   of transparent mouse brain. *Nature Neuroscience*, 14(11), pp.1481–1488. Available at:
688   http://dx.doi.org/10.1038/nn.2928.

689 Hartnett, M.E., 2015. Pathophysiology and Mechanisms of Severe Retinopathy of Prematurity.
690   *Ophthalmology*, 122(1), pp.200–210. Available at:
691   http://linkinghub.elsevier.com/retrieve/pii/S0161642014006940.

692 Hida, K. et al., 2004. Tumor-associated endothelial cells with cytogenetic abnormalities. *Cancer*
693   *research*, 64(22), pp.8249–55. Available at:
694   http://www.ncbi.nlm.nih.gov/pubmed/15548691.

695 Hou, B. et al., 2015. Scalable and DiI-compatible optical clearance of the mammalian brain.
696   *Frontiers in Neuroanatomy*, 9(February), p.19. Available at:
697   http://www.pubmedcentral.nih.gov/articlerender.fcgi?artid=4338786&tool=pmcentrez&rend
698   ertype=abstract.

699 Huber, G. et al., 2009. Spectral domain optical coherence tomography in mouse models of
700   retinal degeneration. *Investigative ophthalmology & visual science*, 50, pp.5888–5895.

701 Jakobsson, L. et al., 2010. Endothelial cells dynamically compete for the tip cell position during
702   angiogenic sprouting. *Nature Cell Biology*, 12(10), pp.943–953. Available at:
703   http://www.nature.com/doifinder/10.1038/ncb2103.

704 Kearney, J.B. & Bautch, V.L., 2003. In Vitro Differentiation of Mouse ES Cells: Hematopoietic
705   and Vascular Development. *Methods in Enzymology*, 365, pp.83–98.

706 Kondoh, M. et al., 2013. Hypoxia-Induced Reactive Oxygen Species Cause Chromosomal
707   Abnormalities in Endothelial Cells in the Tumor Microenvironment R. Morishita, ed. *PLoS*
708   *ONE*, 8(11), p.e80349. Available at: http://dx.plos.org/10.1371/journal.pone.0080349.

709 Kubota, Shimpei I., Kei Takahashi, Jun Nishida, Yasuyuki Morishita, Shogo Ehata, Kazuki
710 Tainaka, Kohei Miyazono, and Hiroki R. Ueda., 2017. Whole-body profiling of cancer metastasis
711 with single-cell resolution. *Cell reports* 20, no. 1: 236-250.
712

713 Lawson, N.D. & Weinstein, B.M., 2002. In Vivo Imaging of Embryonic Vascular Development
714   Using Transgenic Zebrafish. *Developmental Biology*, 248(2), pp.307–318.

715 Liebmann, T., Renier, N., Bettayeb, K., Greengard, P., Tessier-Lavigne, M. & Flajolet, M., 2016.
716   Three-Dimensional Study of Alzheimer's Disease Hallmarks Using the iDISCO Clearing
717   Method. *Cell Reports*, 16(4), pp.1138–1152.

718 Liebmann, T., Renier, N., Bettayeb, K., Greengard, P., Tessier-Lavigne, M. & Correspondence,
719   M.F., 2016. Three-Dimensional Study of Alzheimer's Disease Hallmarks Using the iDISCO
720   Clearing Method.

721 Milde, F., Lauw, S., Koumoutsakos, P. and Iruela-Arispe, M.L., 2013. The mouse retina in 3D:
722 quantification of vascular growth and remodeling. *Integrative Biology*, 5(12), pp.1426-1438.

723 Motoike, T. et al., 2000. Universal GFP for the study of vascular development. *Genesis*, 28,
724   pp.75–81.

725 Murray, E., Cho, J.H., Goodwin, D., Ku, T., Swaney, J., Kim, S.Y., Choi, H., Yoon Park,J.,
726 Hubbert, A., McCue, M., Gyun Park, Y., Vassallo, S., Bakh, N., Frosch,M., Wedeen, V J.,
727 Seung, H.S., Chung, K., 2015. Simple, scalable proteomic imaging for high dimensional profiling
728 of intact systems. Cell 63(6):1500-14. doi: 10.1016/j.cell.2015.11.025. PubMed PMID: 26638076

729 Muzumdar, M.D. et al., 2007. A global double-fluorescent Cre reporter mouse. *genesis*, 45(9),
730 pp.593–605. Available at: http://doi.wiley.com/10.1002/dvg.20335.

731 Narayanan, S.P. et al., 2014. Arginase 2 deficiency reduces hyperoxia-mediated retinal
732 neurodegeneration through the regulation of polyamine metabolism. *Cell Death and
733 Disease*, 5, p.e1075. Available at: http://www.nature.com/doifinder/10.1038/cddis.2014.23.

734 Nentwich, M.M. & Ulbig, M.W., 2015. Diabetic retinopathy - ocular complications of diabetes
735 mellitus. *World journal of diabetes*, 6(3), pp.489–99. Available at:
736 http://www.pubmedcentral.nih.gov/articlerender.fcgi?artid=4398904&tool=pmcentrez&rend
737 ertype=abstract.

738 Nicoli, S. et al., 2010. MicroRNA-mediated integration of haemodynamics and Vegf signalling
739 during angiogenesis. *Nature*, 464(7292), pp.1196–1200. Available at:
740 http://www.nature.com/doifinder/10.1038/nature08889.

741 Pietzsch, T. et al., 2015. BigDataViewer: visualization and processing for large image data sets.
742 *Nature Methods*, 12(2012), pp.481–483. Available at:
743 http://www.nature.com/doifinder/10.1038/nmeth.3392.

744 Preibisch, S. et al., 2014. Efficient Bayesian-based multiview deconvolution. *Nature methods*,
745 11(6), pp.645–8. Available at: http://dx.doi.org/10.1038/nmeth.2929.

746 Renier, N. et al., 2014. iDISCO: A Simple, Rapid Method to Immunolabel Large Tissue Samples
747 for Volume Imaging - suppl original. *Cell*, 159. Available at:
748 http://www.sciencedirect.com/science/article/pii/S0092867414012975.

749 Renier, N. et al., 2016. Mapping of Brain Activity by Automated Volume Analysis of Immediate
750 Early Genes. *Cell*, 165(7), pp.1789–1802.

751 Reynaud, E.G. et al., 2014. Guide to light-sheet microscopy for adventurous biologists. *Nature
752 Methods*, 12(1), pp.30–34. Available at: http://dx.doi.org/10.1038/nmeth.3222.

753 Rezzola, S. et al., 2013. A novel exvivo murine retina angiogenesis (EMRA) assay.
754 *Experimental Eye Research*, 112, pp.51–56.

755 Richardson, D.S. & Lichtman, J.W., 2015. Clarifying Tissue Clearing. *Cell*, 162(2), pp.246–257.
756 Available at: http://linkinghub.elsevier.com/retrieve/pii/S0092867415008375.

757 Sawamiphak, S., Ritter, M. & Acker-Palmer, A., 2010. Preparation of retinal explant cultures to
758 study ex vivo tip endothelial cell responses. *Nature protocols*, 5(10), pp.1659–1665.
759 Available at: http://dx.doi.org/10.1038/nprot.2010.130.

760 Schindelin, J. et al., 2012. Fiji: an open-source platform for biological-image analysis. *Nature
761 methods*, 9(7), pp.676–82. Available at: http://www.nature.com.ezp-
762 prod1.hul.harvard.edu/nmeth/journal/v9/n7/full/nmeth.2019.html.

763 Schmid, B. et al., 2010. A high-level 3D visualization API for Java and ImageJ. *BMC
764 Bioinformatics*, 11(1), p.274. Available at:
765 http://bmcbioinformatics.biomedcentral.com/articles/10.1186/1471-2105-11-274.

766 Schoors, S. et al., 2014. Incomplete and transitory decrease of glycolysis A new paradigm for
767 anti-angiogenic therapy? *Cell Cycle*, 131, pp.16–22.

768 Sommer, C. et al., 2011. Ilastik: Interactive learning and segmentation toolkit. In *2011 IEEE

769   *International Symposium on Biomedical Imaging: From Nano to Macro.* IEEE, pp. 230–233.
770   Available at: http://ieeexplore.ieee.org/lpdocs/epic03/wrapper.htm?arnumber=5872394.

771   Srinivasan, V.J. et al., 2006. Noninvasive volumetric imaging and morphometry of the rodent
772   retina with high-speed, ultrahigh-resolution optical coherence tomography. *Investigative*
773   *Ophthalmology and Visual Science*, 47, pp.5522–5528.

774   Stahl, A. et al 2010; The Mouse Retina as an Angiogenesis Model. *Invest. Ophthalmol. Vis. Sci.*
775   2010;51(6):2813-2826. doi: 10.1167/iovs.10-5176.

776   Stelzer, E.H.K., 2014. Light-sheet fluorescence microscopy for quantitative biology. *Nature*
777   *Methods*, 12(1), pp.23–26. Available at: http://dx.doi.org/10.1038/nmeth.3219.

778   Del Toro, R. et al., 2010. Identification and functional analysis of endothelial tip cell-enriched
779   genes. *Blood*, 116(19), pp.4025–4033.

780   Treweek, J.B. et al., 2015a. Whole-body tissue stabilization and selective extractions via tissue-
781   hydrogel hybrids for high-resolution intact circuit mapping and phenotyping. *Nature*
782   *Protocols*, 10, pp.1860–1896. Available at: http://dx.doi.org/10.1038/nprot.2015.122.

783   Treweek, J.B. et al., 2015b. Whole-body tissue stabilization and selective extractions via tissue-
784   hydrogel hybrids for high-resolution intact circuit mapping and phenotyping. *Nature*
785   *Protocols*, 10, pp.1860–1896.

786   Ubezio, B. et al., 2016. Synchronization of endothelial Dll4-Notch dynamics switch blood
787   vessels from branching to expansion. *eLife*, 5, pp.186–193. Available at:
788   http://www.ncbi.nlm.nih.gov/pubmed/27074663.

789   Udan, R.S. et al., 2014. Quantitative imaging of cell dynamics in mouse embryos using light-
790   sheet microscopy. *Development*, 141(October), pp.4406–4414. Available at:
791   http://dev.biologists.org/cgi/doi/10.1242/dev.111021.

792   Usui, Y. et al., 2015. Neurovascular crosstalk between interneurons and capillaries is required
793   for vision. *The Journal of clinical investigation*, 125(6), pp.2335–46. Available at:
794   http://www.ncbi.nlm.nih.gov/pubmed/25915585.

795   Verheyen, A. et al., 2012. Systemic anti-vascular endothelial growth factor therapies induce a
796   painful sensory neuropathy. *Brain*, 135, pp.2629–2641.

797   Versaevel, M., Grevesse, T. & Gabriele, S., 2012. Spatial coordination between cell and nuclear
798   shape within micropatterned endothelial cells. *Nature Communications*, 3, p.671. Available
799   at: http://www.nature.com/doifinder/10.1038/ncomms1668.

800   Wang, Y. et al., 2010. Ephrin-B2 controls VEGF-induced angiogenesis and lymphangiogenesis.
801   , 465(May).

802   Yang, B. et al., 2014. Single-Cell Phenotyping within Transparent Intact Tissue through Whole-
803   Body Clearing. *Cell*, pp.1–14. Available at: http://dx.doi.org/10.1016/j.cell.2014.07.017.

804   Yuntao, X., Ivanovska, I.L., Zhu, K., Smith, L., Irianto, J., Pfeifer, C.R., Alvey, C. 2018. Nuclear
805   rupture at sites of high curvature compromises retention of DNA repair factors. *J Cell Biol* 217,
806   no. 11: 3796-3808.

807

808

809   **Figure Legends**

810   **Figure 1: Imaging of the whole eye using light sheet microscopy. a,** Schematic of retina

811   preparation for imaging. For conventional confocal microscopy, four incisions are made to

812   enable flat-mounting of the retina onto a cover slip. For LSFM, pieces of the retina are

813   suspended and imaged from a right angle. **b**, Maximum intensity projection (MIP) of a P15

814   mouse eyeball (z = 274 slices). Vessels were visualized with IsoB4 staining. Scale bar, 500 μm.

815   **c,** 3D-rendered image of the adult iris microvasculature (z = 263 slices). Vessels were

816   visualized with IsoB4 (yellow arrows). Scale bar, 250 μm. **d,** MIP of the optic nerve. Vessels

817   were visualized with IsoB4 staining (z = 176 slices). Scale bar, 50 μm. **e,** MIP of a cross section

818   of a P10 mouse retina. Vessels were visualized with IsoB4 staining. Scale bar, 100 μm. **f,** MIP

819   of a whole P10 mouse retina suspended and imaged intact (z = 176 slices). Vessels were

820   visualized with IsoB4 staining. Scale bar, 500 μm. See supplementary figure 1 for additional

821   images.

822   **Figure 2: 3D reconstruction of nerves and vessels in one image. a**, Schematic of an

823   eyeball. **b**, Schematic of the retina and its cell types. **c,** Retinal eye cups expressing yellow

824   fluorescent protein, YFP (green) were harvest from Thy1-YFP mice and stained with Isolectin

825   IB4 (red). The retinal eye cups were mounted and imaged with LSFM. **d,** enlarged region of c. **e,**

826   Representative image of an eyeball before clearing (left panel), and an eyeball after PACT

827   clearing (right panel). The circle around the cleared eyeball depicts the outline of the eyeball.

828   Scale bar, 2 mm. **f,** Draq5 staining (magenta) visualizes the inner nuclear layer (INL) and outer

829   nuclear layer (ONL) of the adult mouse PACT cleared retina. Vessels were visualized by IsoB4

830   staining (green). **g,** Tuj1 (green) and calbindin (red) visualize the ganglion and horizontal cells in

831   the mouse PACT cleared retina. **h**, Smooth muscle actin (SMA, red) and Collagen IV staining

832   (Coll.IV, green) visualize the three vascular layers and smooth muscle cells in the mouse PACT

833   cleared retina. Scale bars, 50 μm.

834 **Figure 3. Vessel depth distortion in confocal due to flatmounting. a,** Schematic showing

835 the correlative LSFM-Confocal imaging approach used to quantify vessel distortion incurred by

836 flatmounting. **b**, the same large vessel segment imaged first with LSFM then confocal (surface

837 rendered in Imaris). By orienting with the surrounding vessel connections to determine the

838 plexus plane (equivalent to the XY plane in confocal) and the plane perpendicular to it ("perp

839 plane"), which is equivalent to the Z plane in confocal, comparative width (W) and depth (D)

840 measurements can be made of the same vessel segment. **c**, cross sectional views of another

841 representative large vessel near the optic nerve shows how the aspect ratio of W and D is

842 shifted to an ellipse in confocal. Near Optic: n = 60 vessels from 6 retinas (7 images). Vascular

843 Front n = 28 vessels in from 4 retinas (4 images) for each confocal and lsfm.

844 **Figure 4: Live-imaging of the retinal vasculature. a,** Single maximum intensity projections

845 (MIP) of an hour time lapse movie show long, slender filopodia, and rapid fusion and

846 disconnection of tip cells at the vascular front of mT/mG x cdh5 (PAC) CreERT2 mice (stars). **b,**

847 MIPs of a time lapse movie reveal the connection between two branches in the capillary plexus

848 (star).

849 **Figure 5: Analysis of three subclasses of OIR vascular tuft. a,** Representative 3D-rendered

850 LSFM images of small (1st row), medium (2nd row), and large (3rd row) tufts showing the

851 vasculature (IsoB4, green) and endothelial nuclei (ERG, magenta), scale bar = 10 μm. For all

852 widefield images, scale bar = 40 μm, yellow box indicates tuft in situ; 4th row **-** representative

853 3D-rendered images showing curved nuclei in a medium tuft, yellow arrows indicate curved

854 nuclei, blue arrows indicate flat nuclei parallel to each other. Scale bar, 10 um. 5th row:

855 correlative LSFM-confocal microscopy of the same tuft reveals the tuft depth distortion (side

856 view) incurred with confocal flatmounting versus LSFM. **b,** The volume of the tufts versus the

857 number of nuclei per tuft. **c,** The number of vessel connections between the tuft and the

858 underlying vascular plexus versus the number of nuclei. **d,** Quantification of the number of

859   curved nuclei per tuft versus the total number of total nuclei per tuft. **e**, quantifications of tuft

860   depths per subclass size in LSFM vs confocal images, significant difference shown using

861   unpaired t test, *** means P <0.0001.

862   **Figure 6. Knotted morphology of neovascular tufts revealed with LSFM**. **a,d,g,**

863   representative 3D-rendered images (generated using IMARIS software) of large (upper panel),

864   medium and small tufts showing the vasculature (IsoB4, green) and endothelial nuclei (ERG,

865   red) from rotational movies S14,15 See Supp. Fig. 2a for further views from different angles of

866   the large tufts. White dashed arrows indicates a hole through the tuft. Scale bar, 30 μm. **b,**

867   widefield LSFM of OIR retina demonstrates that the knotted morphology is hard to discern from

868   afar. **c**, detailed 3D clipping plane and 3D rotational drawings of an individual knot reveal a

869   figure of eight structure with two clear holes through the tuft aswell a vessel connecting from the

870   upper, vitreous facing surface of the tuft to the plexus below (blue star). Stars mark

871   corresponding regions from the illustration to the images - lower tuft loop nearer plexus (yellow

872   star), upper tuft loop nearer vitreous (red star). See also Suppl. Fig. 2b for detailed 3D drawings

873   made from each rotational view of this tuft with clipping planes, and Movie S13. **e,h,** 3D

874   sketches made from rotational movies S16,17 to better elucidate nuclei**:** blue nuclei - bottom of

875   tuft (near plexus), red nuclei – middle of tuft (in **e**), top of tuft (facing vitreous) in **h**, yellow nuclei

876   - top of tuft (facing vitreous) in **e**,**f**,**i,** schematic illustrating the swirling tuft morphology observed

877   in **d-h** with three layers for the medium tuft (**f**) and two for the small one (**i**).

878   **Figure 7.** OIR live imaging **a,** Maximum intensity projections (MIPs) of a time lapse movie of a

879   retinal tuft of a mouse in the oxygen-induced retinopathy (OIR) model visualize short, rapidly

880   extending and retracting filopodia as compared to control retinas (stars). **b,** MIPs of a time lapse

881   movie of mouse retinal vasculature in the OIR model reveal cell shuffling in real-time (arrow). **c,**

882   MIPs of a time lapse movie of mouse retinal vasculature in the OIR model reveal abnormal

883   vessel growth in real-time. Scale bar, 20 μm. **d,** the maximum length that each filopodia reached

884 was measured for each filopodia over time in P5 and OIR conditions. **e,** the total time that each

885 filopodia was present during the experiment; this time is calculated from when one filopodia

886 appeared and then disappeared. **f,** speed of extension and retraction of filopodia were

887 calculated for P5 and OIR conditions. Total n= 67 and 23 filopodia in 8 and 3 cropped movies

888 from 3 independent P5 and 1 OIR experiment.

889 **Supplemental Figure Legends**

890

891 **Supplemental Figure 1 related to Figure 1.** **a,** Maximum intensity projection of the iris

892 microvasculature of two-week old mouse, LSFM. Vessels were visualized with IsoB4 (green).

893 Scale bar, 200 µm; **b,** the full unprocessed retinal image used for the cropped figure in Fig. 1e.

894 **c,** P12 retina stained using anti-CD31(Alexa 555), Anti-Erg (alexa488) and anti-Golgi (Golph4,

895 Alexa 647) imaged using LSFM, Scale bar is 10 µm. **d**, P12 Retina stained for CollagenIV

896 followed by LSFM imaging. Scale bar is 20 µm. **e,** lifeAct (green) mouse retinas stained for

897 vessels (IsoB4 - red), merged images shows the overlap between these two channels together

898 with the plot profile (**g**) of the selected area and the yellow arrow (**f**). **h,** the same channels were

899 deconvolved using Huygens and **i,** the same area was plotted to compare the image resolution

900 after deconvolution. Values were normalized to the maximum fluorescence intensity across both

901 images at each pixel.

902

903 **Supplemental Figure 2 related to Figure 6. a**, extended rotational views to see knotted

904 structure from different angles of tuft 1 and 2 in Fig. 6a taken from movies S14, S15. **b**, 3D

905 illustration (made with uMake software) while viewing the tuft with curved nuclei (from Fig. 6c

906 and movie S13) from top to bottom with clipping planes to better understand how the knot

907 topology changes through the tuft from the vitreous to the plexus side. Blue star indicates the

908 unexpected vessel joining the top (vitreous facing) surface of the tuft to the plexus below. **c,** a

909   second example of a medium tuft with a swirl structure and clear protrusive sprout-like

910   morphology to the upper vitreous facing end point of the swirl.

911

912   **Movie Legends**

913   **Movie S1.** 3D-rendered LSFM z-stack of retinal eye cups expressing yellow fluorescent protein,

914   YFP (green) harvest from Thy1-YFP mice and stained with Isolectin IB4 (red).

915   **Movie S2.** 3D-rendered LSFM z-stack of all nuclei (Draq5, magenta) visualizes the inner

916   nuclear layer and outer nuclear layer of the adult mouse retina. Vessels were visualized by

917   IsolectinB4 staining (green). The retinal pigment epithelium emits green autoflourescence.

918   **Movie S3**. 3D-rendered LSFM z-stack of an adult mouse retina stained for Tuj1 (green) and

919   horizontal cells (calbindin, red) visualizing the ganglion cells and horizontal cells, respectively.

920   **Movie S4.** 3D-rendered LSFM z-stack of an adult mouse retina stained for Smooth Muscle Actin

921   (SMA, red) and CollagenIV staining (ColIV, green) visualizes the three vascular layers and

922   smooth muscle cells in the mouse retina.

923   **Movie S5.** An hour time lapse LSFM movie showing long, slender filopodia, and rapid "kiss and

924   run" fusion and disconnection of tip cells at the vascular front of mT/mG x cdh5 (PAC) CreERT2

925   mice. Frame rate: 1 image/45 sec.

926   **Movie S6.** A 9 hour time lapse LSFM movie showing a connection between two branches in the

927   capillary plexus of mT/mG x cdh5 (PAC) CreERT2 mice. Frame rate: 1 image/20 min.

928   **Movie S7.** Representative tracking of a short-lived actin-rich bundle in life-Act-EGFP retina mice

929   imaged with LSFM (7 min). The tracking was performed manually using Manual Tracking plugin

930   in Fiji/ImageJ.

931   **Movie S8.** Representative tracking of a longer-lived actin-rich bundle in life-Act-EGFP retina

932   mice imaged with LSFM (30 min). The tracking was performed manually using Manual Tracking

933   plugin in Fiji/ImageJ.

934   **Movie S9.** Representative tracking of a long-lived actin-rich bundle track in life-Act-EGFP retina

935   mice imaged with LSFM (40 min). The tracking was performed manually using Manual Tracking

936   plugin in Fiji/ImageJ.

937   **Movie S10.** 3D-rendered LSFM z-stack of a 'small tuft' from an OIR mouse retina stained for

938   blood vessels (IsolectinB4, green), and the nuclear marker ERG (magenta). The z-stack was

939   rendered in Imaris.

940   **Movie S11.** 3D-rendered LSFM z-stack of a 'medium tuft' from an OIR mouse retina stained for

941   blood vessels (IsolectinB4, green), and the nuclear marker ERG (magenta). The z-stack was

942   rendered in Imaris.

943   **Movie S12.** 3D-rendered LSFM z-stack of a 'large tuft' from an OIR mouse retina stained for

944   blood vessels (IsolectinB4, green), and the nuclear marker ERG (magenta). The z-stack was

945   rendered in Imaris.

946   **Movie S13.** 3D-rendered z-stack showed a curved nuclei in a 'medium tuft' from an OIR mouse

947   retina stained for blood vessels (IsolectinB4, green), and the nuclear marker ERG (magenta).

948   The z-stack was rendered in Imaris.

949   **Movie S14.** 3D-rendered LSFM z-stack deconvolved in Huygens then reconstructed with

950   surface rendering in Imaris of 'Large tuft 1' from an OIR mouse retina stained for blood vessels

951   (IsolectinB4, green), and the nuclear marker ERG (red).

952   **Movie S15.** 3D-rendered LSFM z-stack deconvolved in Huygens then reconstructed with

953   surface rendering in Imaris of 'Large tuft 2' from an OIR mouse retina stained for blood vessels

954   (IsolectinB4, green), and the nuclear marker ERG (red).

955   **Movie S16.** 3D-rendered LSFM z-stack deconvolved in Huygens then reconstructed with

956   surface rendering in Imaris of a 'small tuft' from an OIR mouse retina stained for blood vessels

957   (IsolectinB4, green), and the nuclear marker ERG (red).

958   **Movie S17.** 3D-rendered LSFM z-stack deconvolved in Huygens then reconstructed with

959   surface rendering in Imaris of 'a Medium swirl tuft' from an OIR mouse retina stained for blood

960   vessels (IsolectinB4, green), and the nuclear marker ERG (red).

961   **Movie S18.** A 2.5 hour time lapse movie of a retinal tuft of a mouse in the OIR model using

962   mT/mG x cdh5 (PAC) CreERT2 mice visualize short, rapidly extending and retracting filopodia

963   as compared to control retinas. Frame rate: 1 image/minute.

964   **Movie S19.** A 2.5 hour time lapse movie of mouse retinal vasculature in the OIR model using

965   mT/mG x cdh5 (PAC) CreERT2 mice reveal cell shuffling in real-time. Frame rate: 1

966   image/minute.

967   **Movie S20.** A 2.5 hour time lapse movie of mouse retinal vasculature in the OIR model using

968   mT/mG x cdh5 (PAC) CreERT2 mice reveal abnormal vessel growth in real-time. Frame rate: 1

969   image/minute.

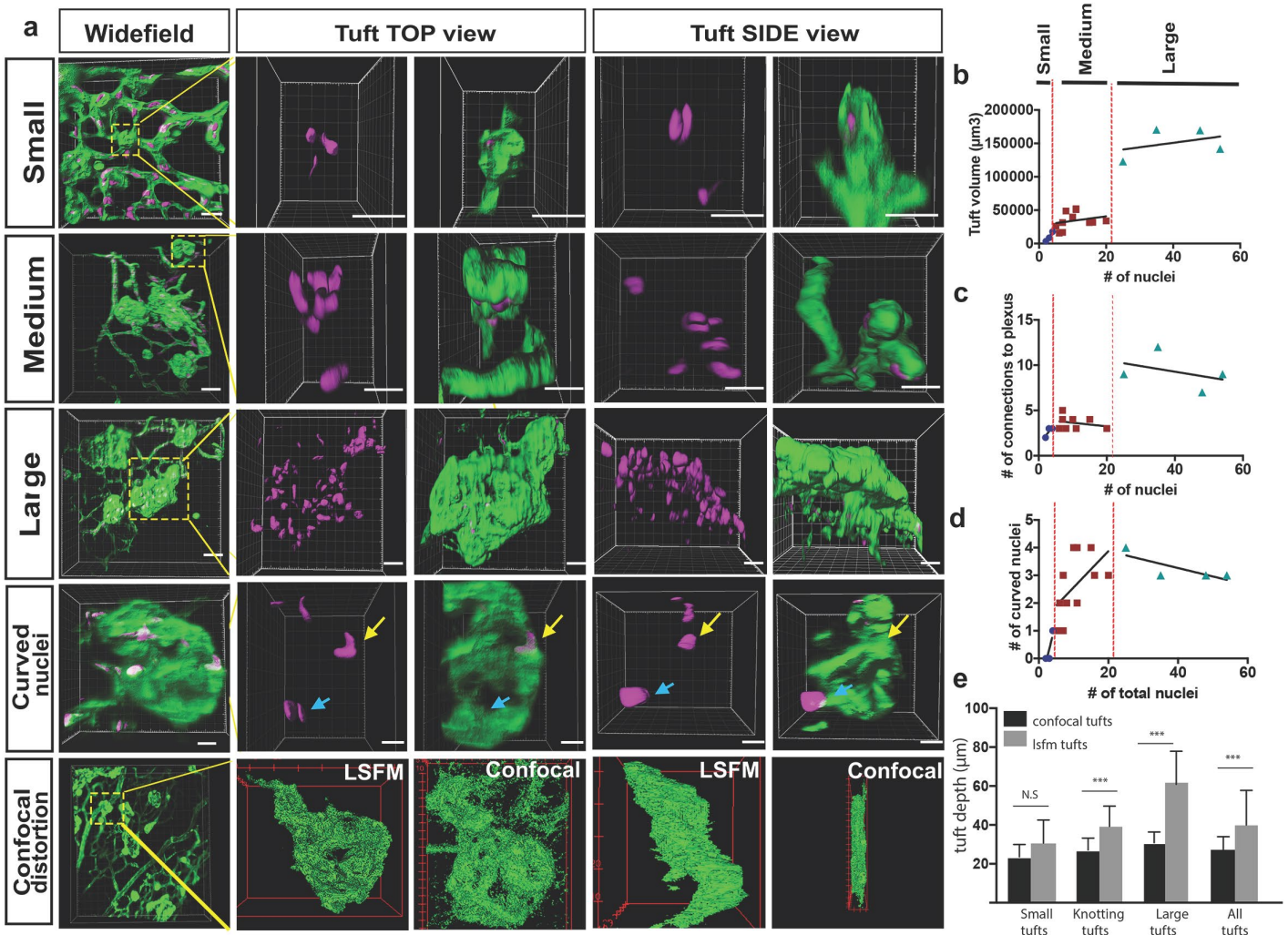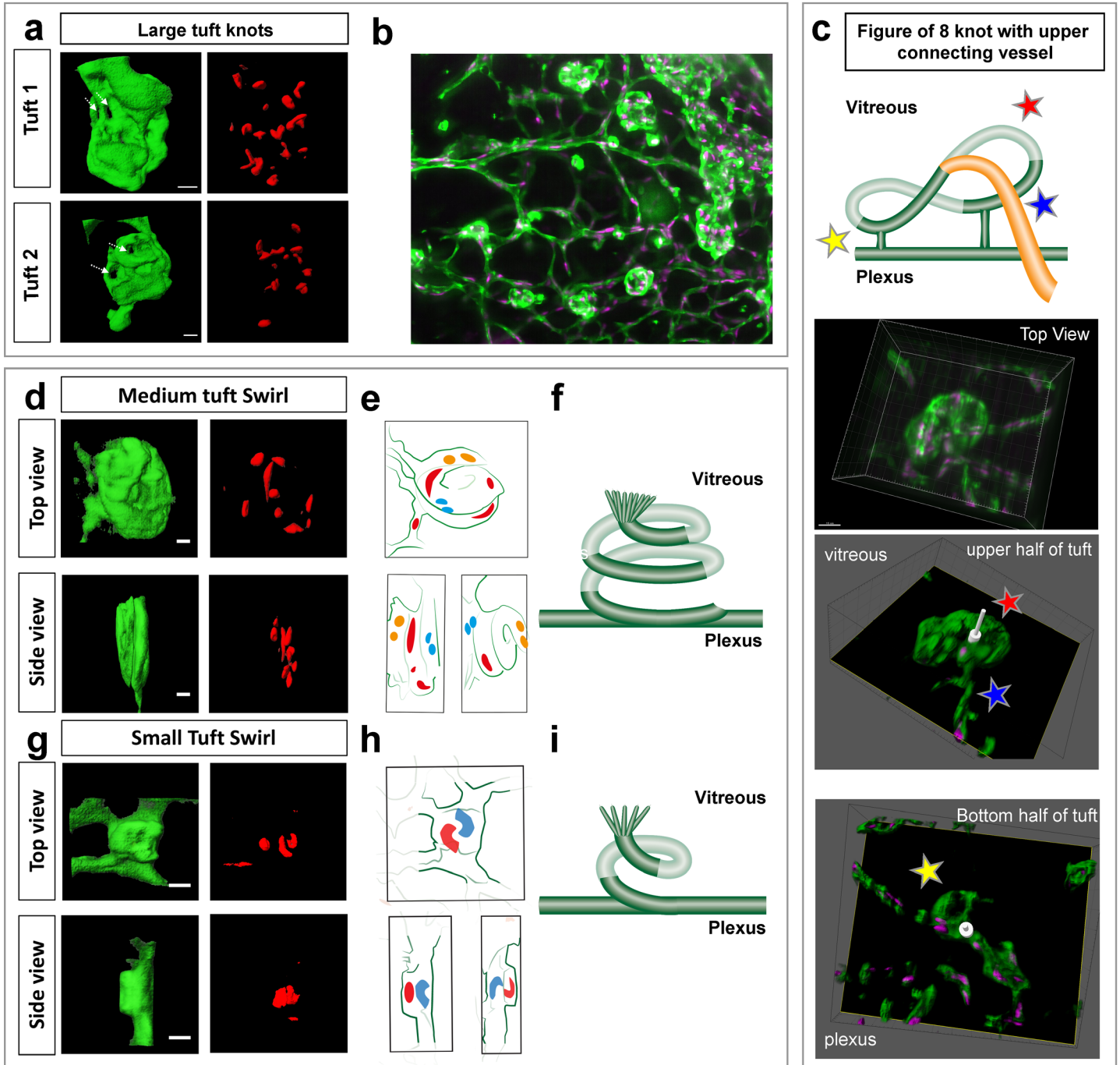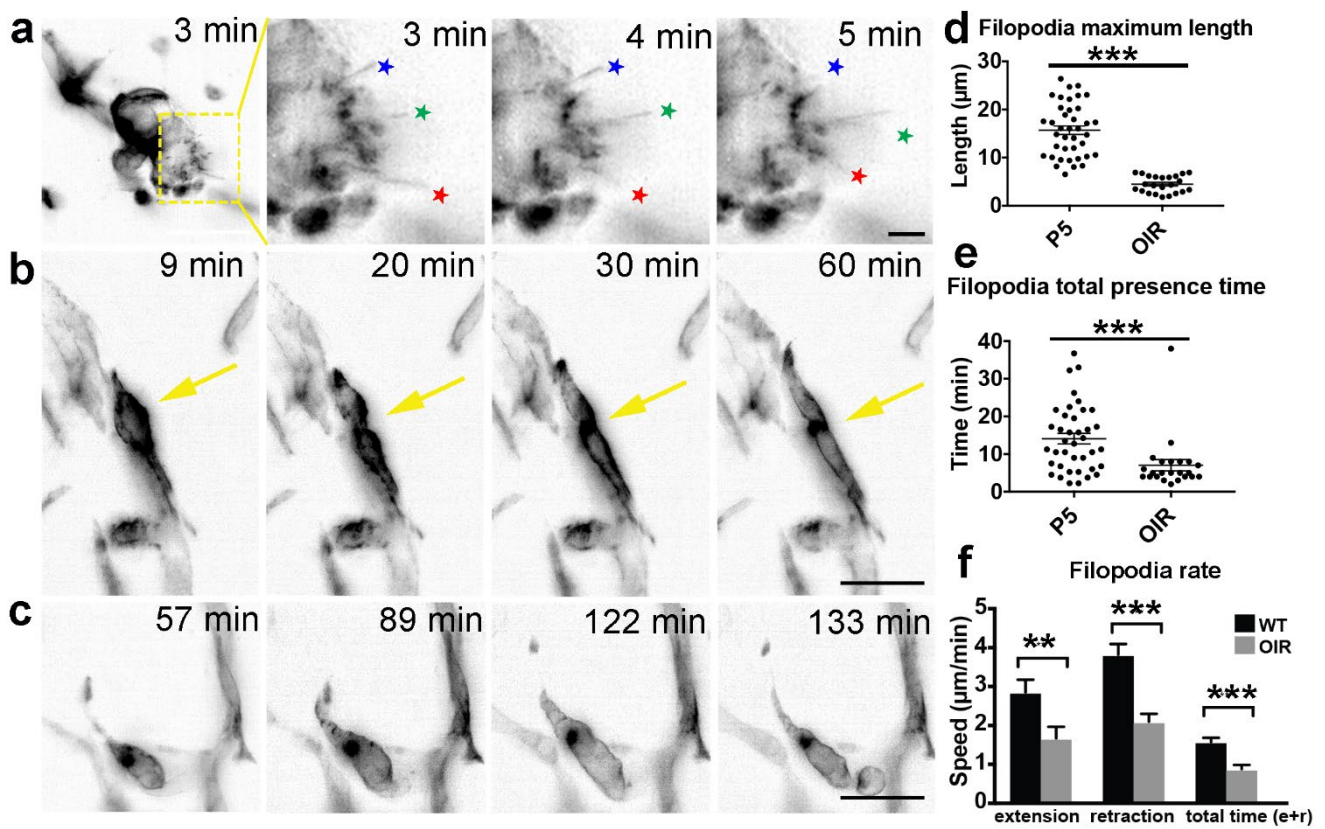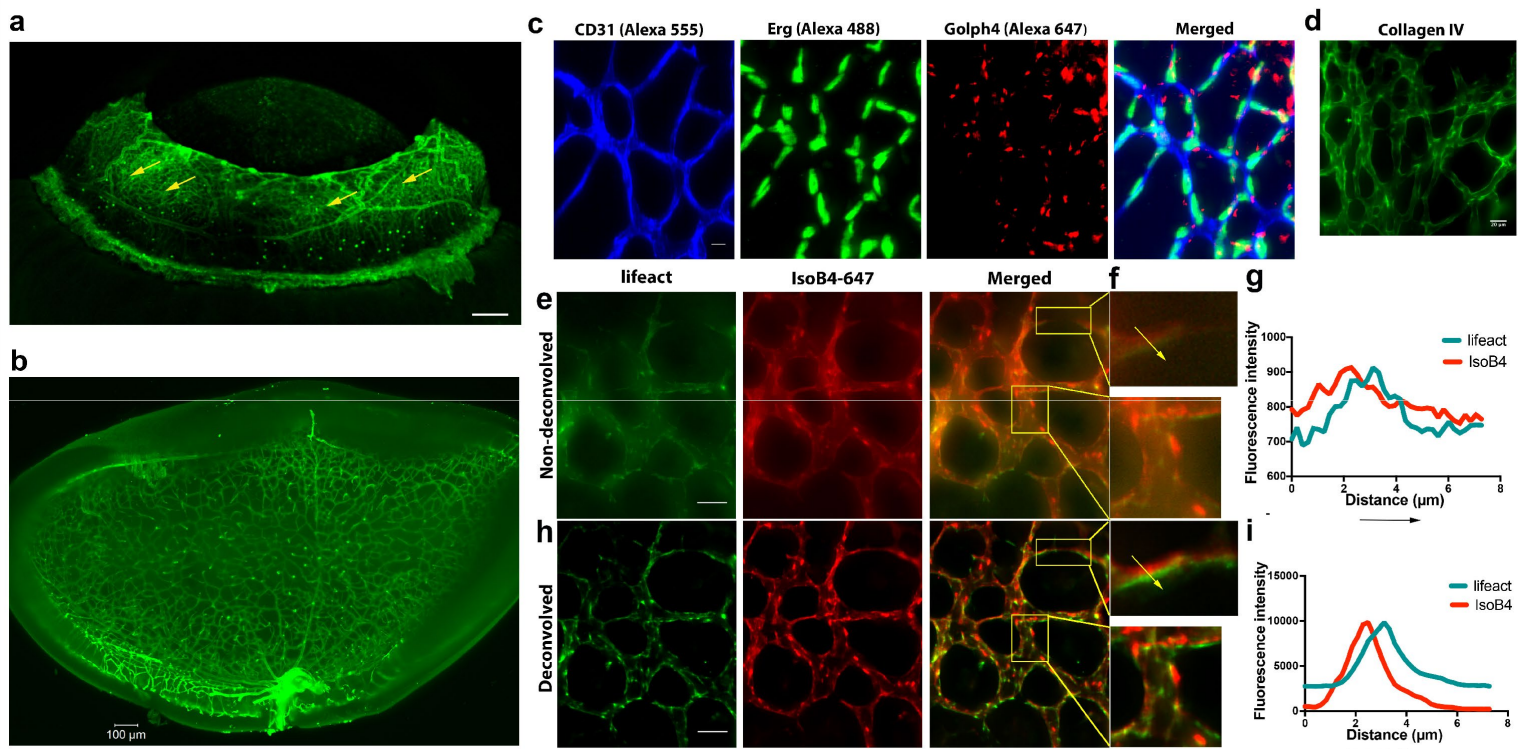970

Figure 1.
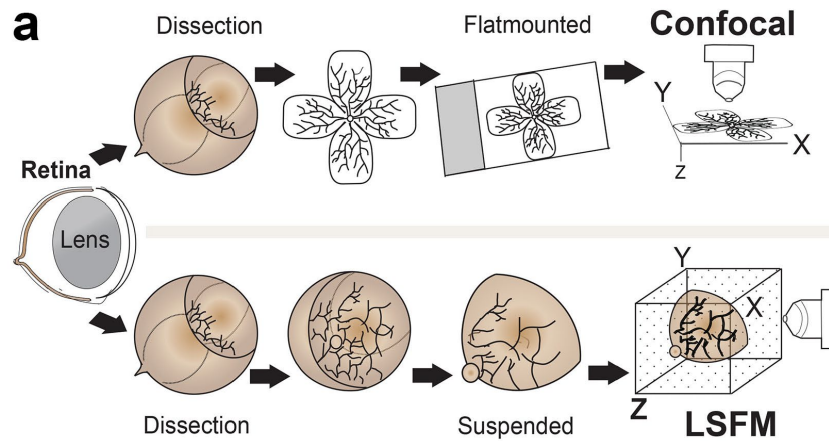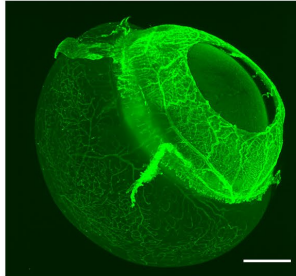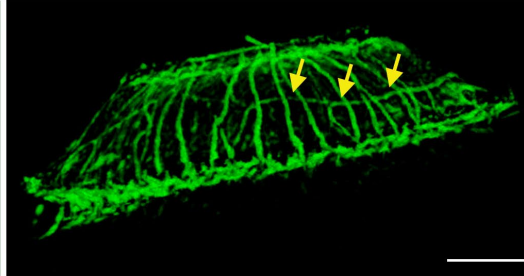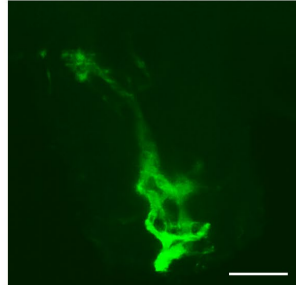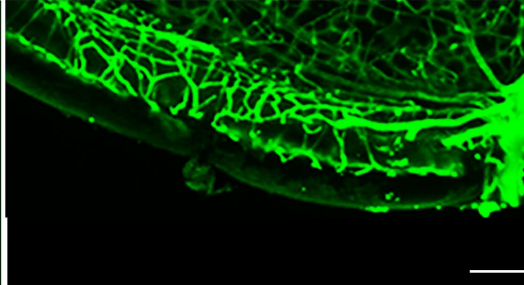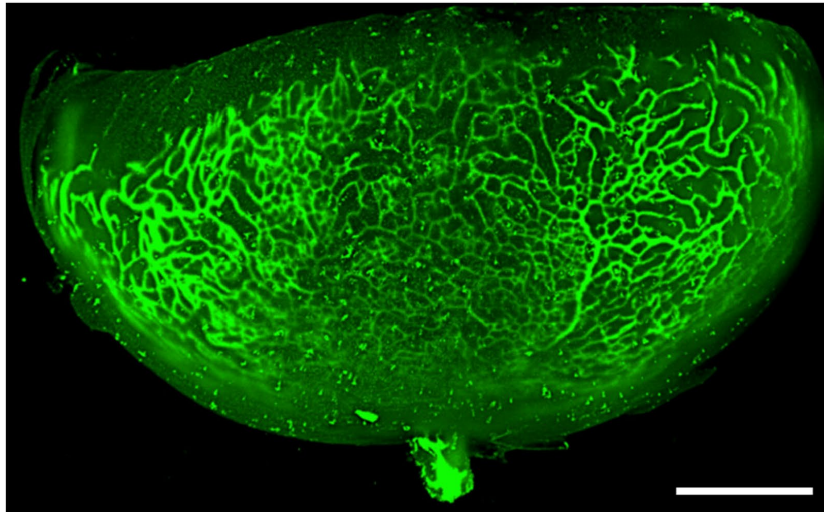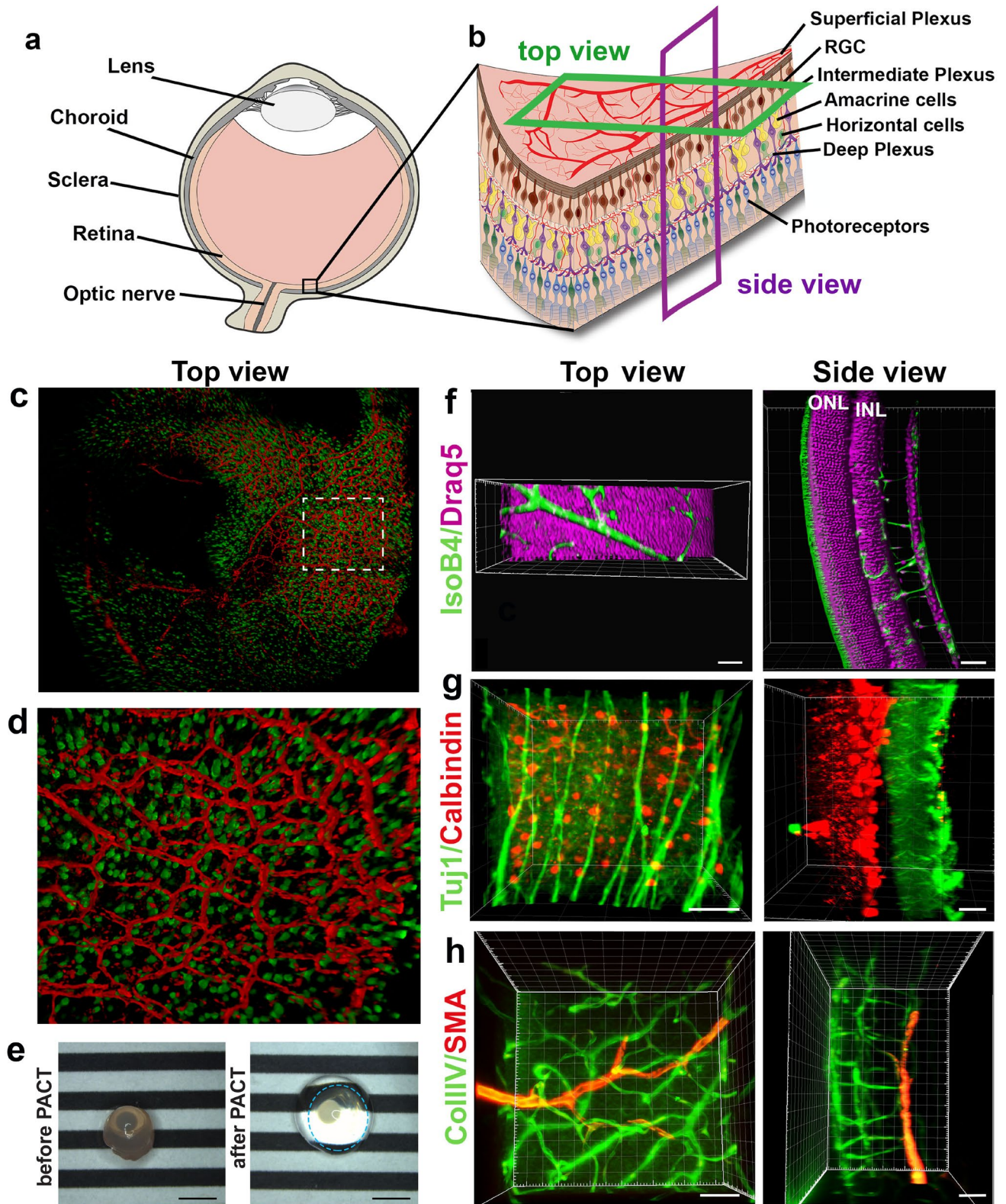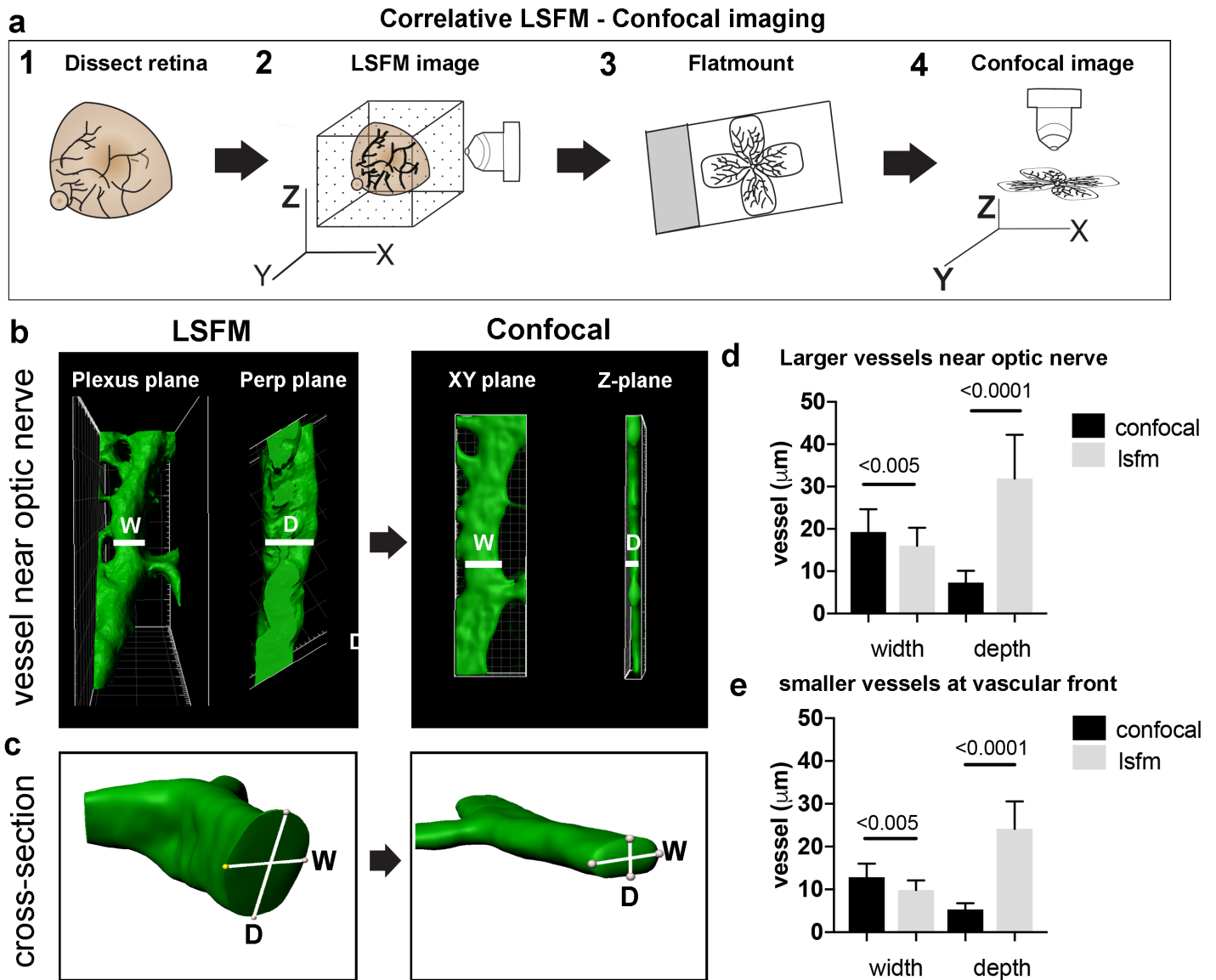
Figure 2.

Figure 3.

Figure 4.
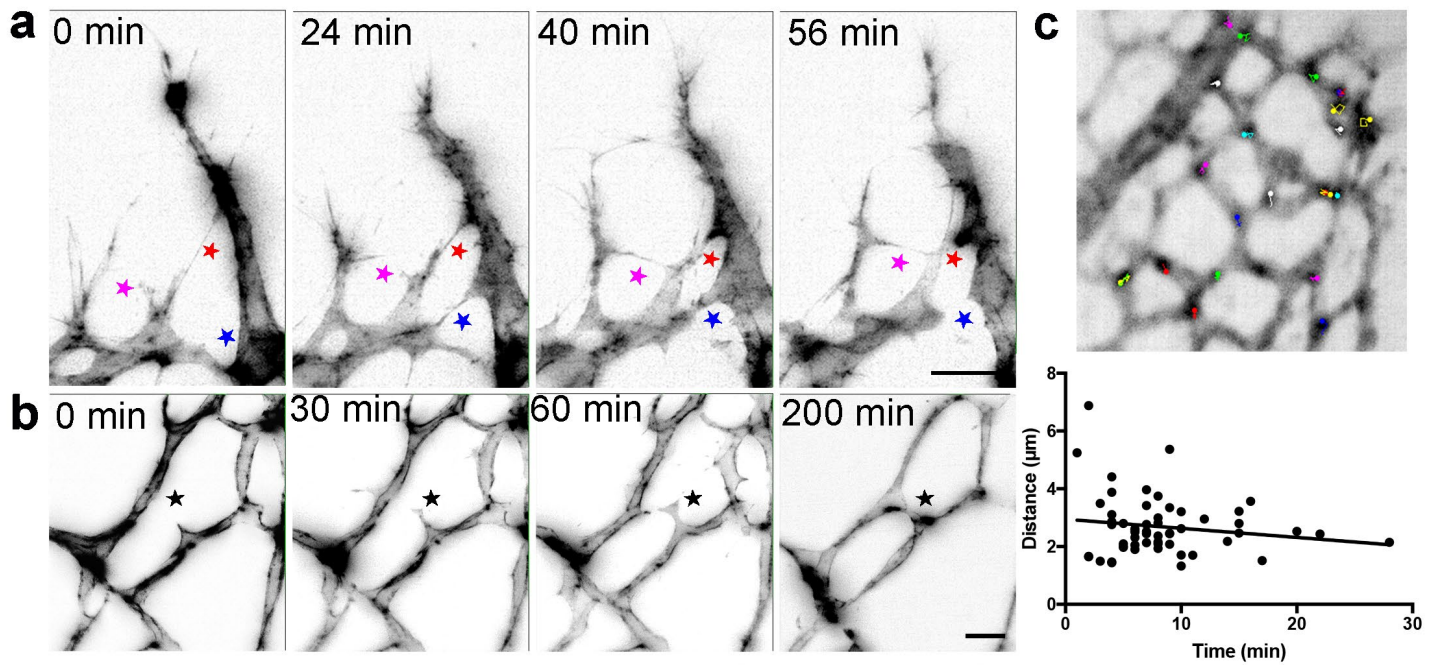
Figure 5.

Figure 6.

Figure 7.

Supp. Figure 1.

Supp. Figure 2.